THESIS FOR THE DEGREE OF LICENTIATE OF ENGINEERING

Mechanical Properties, Microstructures and Defects of Tool Steels Fabricated by Additive Manufacturing

MIWEN YUAN

Department of Industrial and Materials Science

CHALMERS UNIVERSITY OF TECHNOLOGY

Gothenburg, Sweden 2021

Mechanical Properties, Microstructures and Defects of Tool Steels Fabricated by Additive Manufacturing

MIWEN YUAN

Technical report no IMS-2021-6

Department of Industrial and Materials Science
Chalmers University of Technology
SE-412 96 Gothenburg
Sweden Telephone + 46 (0)31-772 1000

Chalmers digitaltryck

Gothenburg, Sweden 2021

Mechanical Properties, Microstructures and Defects of Tool Steels Fabricated by Additive Manufacturing

Miwen Yuan
Department of Industrial and Materials Science
Chalmers University of Technology

Abstract:

Additive Manufacturing (AM) has been gaining significant interest in the manufacturing of metallic materials in the recent years. From a techno-commercial standpoint, tooling is one of the areas with low production volumes with very high demands on part performance and complexity in design are typical, all of which are characteristic for metal AM. In this thesis study, the focus has been on AM of tool steel intended for hot work applications. Tool steels manufactured through laser beam powder bed fusion (LB-PBF) and directed energy deposition (DED) are studied.

A modified H13 hot work tool steel was produced by means of laser beam powder bed fusion (LB-PBF). The effect of two post processing routes, direct tempering (DT) of as-built part and conventional austenitizing followed by tempering (QT), was evaluated with respect to their impact on microstructure and mechanical properties in terms of hardness, tensile properties and impact toughness. The typical microstructure observed in DT condition retained the melt pool boundaries and cellular structure from the as-printed state as well as tempered martensite. A more uniform microstructure including tempered martensite with carbides possibly along lath boundaries was obtained in the QT condition. While comparable hardness and tensile properties were obtained in these two conditions, QT sample exhibited significantly higher impact toughness compared to DT sample due to its higher work hardening ability and strain rate sensitivity originating from the varied microstructure.

For hot-work applications, resistance of the steel to softening at high temperatures is critical and determines the life of the tool. After long term exposure at elevated temperatures, the response of modified H13 after DT and QT treatments was evaluated by means of hardness measurements and microstructural observation. Thermal softening resistance was strongly influenced by the post-AM treatment and the conditions of subsequent exposure at high temperatures. As expected, lesser softening was observed for 550 °C exposure than that for 600 °C. The decrease of hardness was more severe for QT samples. It is hypothesized that finer grain size of ferrite, less coarsened carbides and the cellular structure being preserved contribute to DT samples being more resistant to thermal softening. Evolution of carbides was analyzed by a combination of experiment and simulation using JMatPro software.

For AM tool steels having high hardness, high strength and poor ductility, defects constitute a particularly serious concern. Uddeholm Vanadis 4 Extra (V4E) cold work steel was deposited on a hot work tool steel with a modified H13 composition (Uddeholm Dievar) by DED with varying number of layers. In the as-built state, defects including pores and cracks were found in the deposited zone. The number of both kinds of defects increased with the building height. Three types of pores were identified: large irregular, keyhole and shrinkage pores. Thin Si oxide film (~20 nm) was detected on the internal surface of the larger irregular pores by means of EDX and AES, below which a layer enriched in alloying elements and C was detected. The formation of this type of pore was supposed to be associated with the elemental segregation on the pore surface and insufficient heat input. Solidification cracking was observed as well, especially in the 3rd and 4th layers. Two factors are considered to contribute to higher cracking susceptibility: a) large temperature range for the solidification of V4E steel, simulated by ThermoClac software; b) change in microstructure with the building height from cellular to columnar dendrite.

Keywords: Additive manufacturing, Tool steels, Laser beam powder bed fusion, Directed energy deposition, Post heat treatment, Softening resistance, Carbides, Pores, Solidification cracking.

Preface

The work presented in this licentiate thesis was conducted at the Department of Industrial and Materials Science at Chalmers University of Technology between February 2019 and June 2021. Research has been carried out under the supervision of Professor Yu Cao and Professor Lars Nyborg. The thesis has also been co-supervised by Dr Seshendra Karamchedu and Professor Libin Liu.

List of Appended Papers:

1. **Characteristics of a Modified H13 Hot-work Tool Steel Fabricated by means of Laser Beam Powder Bed Fusion**

   M. Yuan, Y. Cao, S. Karamchedu, S. Hosseini, Y. Yao, J. Berglund, L. Liu, L. Nyborg

   Submitted to journal publication

2. **Study of Defects in Directed Energy Deposited Vanadis 4 Extra Tool Steel**

   M. Yuan, S. Karamchedu, Y. Fan, L. Liu, L. Nyborg, Y. Cao

   Manuscript to be submitted

Table of Contents

Chapter 1 – Introduction

In recent years, more and more attention has been paid to additive manufacturing (AM) technology. Compared with conventional processes, the main advantage of AM technology is that it can manufacture components with complex structures, and the lead time is significantly shortened. The disadvantage is that it cannot produce parts in large quantities like traditional processes. However, in some cases, mass production is not demanded. For example, when producing bones or teeth implants in the human body, AM can produce parts with nearly perfect shapes. Another application example is to repair expensive aerospace parts. In these applications, the research has been focused on processing, microstructure, biocompatibility, mechanical properties at room and elevated temperatures and lightweight issues etc. Optimization of process parameters and materials exploration is still required.

The AM of tool steel is more challenging compared to other types of steels. In AM process, when tool steels cool from high temperature, a martensitic phase with high hardness and low plasticity will be formed owing to the high hardenability originating from high C and alloying element content. Combined with the high thermal stress caused by rapid cooling, some defects (such as hot cracking, delamination and distortion) can be easily formed [1-3]. Besides, pores and lack of fusion are also the common defects in AM components due to the choice of improper process parameters [4]. These defects should be avoided as much as possible because they will greatly reduce the mechanical properties and service life of additively manufactured components. At present, preheating the substrate and optimizing process parameters are the major means to eliminate defects [5]. However, the AM technology for defect-free tool steel components is far from mature.

Hot work steel H13 having high strength with reasonable ductility, good hardenability and thermal cracking resistance is one of the widely used steels in hot stamping tool. In the recent years, there have been some studies on this high strength steel produced by LB-PBF [6-8]. In the published literatures, most of the H13 steels fabricated by LB-PBF are still inferior to the conventional H13 steels in terms of mechanical properties. Slight modification of composition to H13 grade could be a possible way to overcome these drawbacks.

Although the quality of AM-parts can be improved to certain extent by optimizing the processing parameters, most of the as-printed components cannot meet the demands of industry application. Post heat treatments are often necessary for as-built AM parts [9] in order to remove the residual stress and improve their properties. For example, the yield strength of 17-4PH stainless steel produced by LB-PBF was improved from 620 MPa to 1100 MPa after a proper post treatment [10]. It is important to search for suitable post heat treatment for AM parts. In addition, most of the work in literature concern hardness and tensile properties of H13 steel produced by LB-PBF in terms of mechanical properties. Only a few investigations focus on evaluating the softening resistance of AM parts at elevated temperatures [11]. Considering hot working stool steel is exposed to high temperatures during service, it is important to evaluate their thermal softening resistance.

Hot forming is an important and widely used process in the automotive manufacturing segment. Tools in this process are demanded to have a good wear resistance. One major problem in this application is that the generally used hot work tool steel suffers a severe wear when tool is used to forming the un-coated sheet material. In this case, DED is a good choice for the manufacture of larger dies and repair/refurbishment of production dies because of its freedom of material deposition. It provides a potential way to obtain hardfacing of the tools and delay the advent of wear or to repair the worn tools.

In this case, the materials used for hardfacing should have a better wear resistance than the used hot work tool steels. Vanadis 4 Extra (V4E) provided by Uddeholms AB has an outstanding wear resistance in tool steels [19]. In the present study, V4E was employed as the hardfacing material in the DED process on Uddeholm Dievar hot work tool steel.

However, investigations of DED on cold work tool steels in literature are limited due to their poor weldability [12-13]. Cracking and porosity are major problems in the DED of cold work tool steel. Barr et al. [12] reported that the cracks were even found in deposited zone in 1-layer DED samples fabricated with the material of Aermat 100. Most of work in literatures only involved one deposited layer, because cracking still remains a challenge in the multi-layer deposition of cold tool steels. In the present study, 1, 2 and 4 layers were deposited on the bulk of Uddeholm Dievar tool steel to investigate the influence of building height on defect formation.

1.1 Research Objectives

The objectives of this thesis therefore are to investigate two aspects related to AM of tool steel. The first would be to investigate the microstructure and mechanical properties of a modified H13 (M-H13) hot work tool steel manufactured by laser beam powder bed fusion (LB-PBF), and to explore the heat treatment route suitable for M-H13 steel. Softening resistance at elevated temperatures was also evaluated on the material with different post heat treatments. The second objective is to investigate the defect formation and related mechanisms in Uddeholm Vanadis 4 Extra (V4E) cold work tool steel deposited on Uddeholm Dievar tool steel by directed energy deposition (DED).

Chapter 2 – Tool Steels

2.1 Background

From the International Standard EN ISO 4957:1999, tool steel is defined as "Special steels suitable for working or processing of materials, for handling and measuring workpieces and, for this purpose, exhibiting high hardness and wear resistance and/or toughness" [15]. The earliest tool steels were just the ordinary carbon tool steels. The representative steel is Damascus steel, which was welded by layers of high-carbon steels and low-carbon steels [16-17]. It combines the strength of high-carbon steel with the ductility of low-carbon steels. The modern tool steels started from the Mushet special tool steel when Robert Mushet added tungsten to high carbon steel in 1868 [18]. By the beginning of the twentieth century, many complex high-alloy tool steels had been developed. In these steels, tungsten, molybdenum, chromium, vanadium and manganese were common alloying elements. Under various harsh service condition, different tool steels were designed with high hardness and strength, good wear resistance and hot hardness as well as dimensional stability.

It is well known that alloy elements are critical for enhanced properties of tool steels. It is necessary to have a good understanding of the metallurgical effects of these major alloy elements, which are discussed as follows:

Carbon. Before adding any other alloying elements, carbon plays a dominated role in tool steel. It can increase the hardenability of steels and harden the steels by forming martensite. Interstitially dissolved C atoms in crystal lattice can efficiently inhibit the sliding of dislocation lines, which could improve the strength and hardness of steels. Cementite formed between carbon and Fe also has the similar effect. Moreover, the carbides formed by carbon and alloying elements are usually harder than cementite. Hence, these carbides can significantly increase the hardness of tool steel. In general, increasing the carbon content will increase the hardness and wear resistance of steels, but it will sacrifice the ductility and toughness of the steels.

Silicon. Silicon is one of the main deoxidizers in the process of making steels owing to its high affinity with O. Silicon could help to improve the hardenability and softening resistance of steels. When added to hot work tool steels, silicon could contribute to increase in depth of hardening.

Chromium. Chromium in steels generally improves the oxidation resistance and corrosion resistance as well as hardenability of steels. For cold work tool steels, chromium can form carbides to improve wear resistance. When added into hot work tool steels, chromium can increase their softening resistance and hot hardness.

Molybdenum and Tungsten. Both molybdenum and tungsten are important for hot work steels and high-speed steels. The carbides formed are extremely hard, which can efficiently prevent grain growth. This unique property makes them popular in improving the high temperature strength and hot hardness of steels. Molybdenum can also increase the weldability and the tendency of secondary hardening. These two elements are widely used in high-speed steels and hot forming tool steels.

Vanadium. Vanadium is a strong carbide former. The carbides it forms have a high hardness, which will dramatically improve the wear resistance. Vanadium also acts as grain refiner and improves hot hardness. Hence, vanadium is popular in tool steels, especially in hot work steel and high-speed steel.

Manganese. Manganese is a deoxidizer in the process of melting steel. In many cases, manganese is added to steels and bound with S to decrease the detrimental effect of S on weldability. Manganese also

can reduce the critical cooling rate of martensite formation during quenching. It can improve the hardenability of steels and reduce the distortion caused by quenching.

There are also many other important alloy elements (e.g., nickel, copper, cobalt, etc.) in tool steels, which will not be discussed in detail in this section.

2.2 Classifications of Tool Steels

Instead of classification based on the chemical composition, tool steels are often classified based on their properties and applications. According to International standard classification, tool steels are divided into four categories: non-alloy cold work tool steels, alloy cold work tool steels, alloy hot work tool steels and high-speed steels. The composition, properties and applications of various categories are described below.

2.2.1 Non-alloy Cold Work Tool Steels

"Non-alloy" means there is basically no other alloy elements except 0.42% to 1.25% C, 0.10% to 0.40% Si, and 0.10% to 0.80% Mn. The high hardness is attributed to the martensite phase and iron carbides, which are produced by heat treatment. Without the help of other alloy elements, the hardening depth will be just about 3 mm. The grades such as C70U to C120 U (the number in middle represent the ten thousandths of C content) steels belong to shallow hardening steels except C45U steel which does not need heat treatment. The CCT diagram of steel C90U (one grade of non-alloy cold work tool steels) simulated by JMatPro is shown in Figure 1a. The critical cooling rate is about 100 K/s. After water quenching, the hardness at surface can reach 60 HRC while it decreases quickly with the distance from

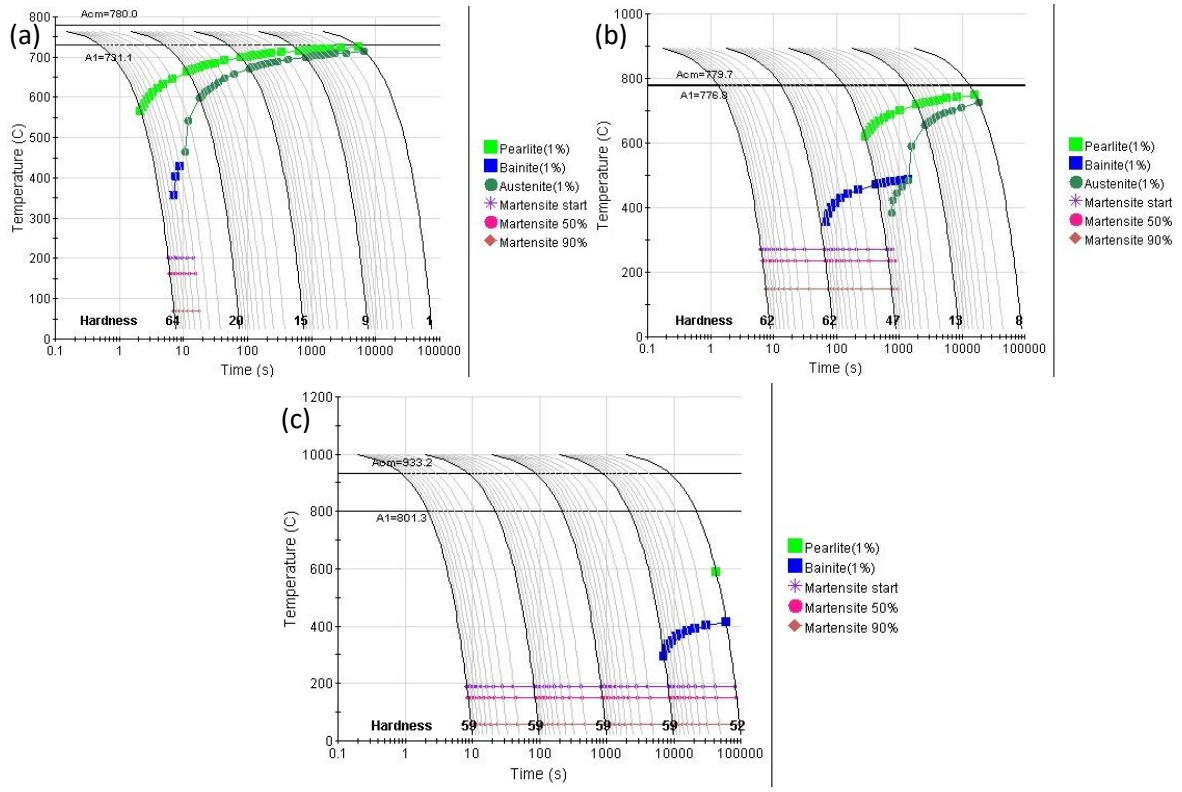

Figure.1 The CCT diagrams simulated by JMatPro. (a) C90U non-alloy tool steel simulated under the condition of austenitizing temperature 780 ℃ and grain size of 10 μm, (b) 60WCrV8 cold work tool steel (910 ℃ and 29 μm), (c) X153CrMoV12 cold work tool steel (1020 ℃ and 80 μm).

the surface. The low price of this type of steels makes it popular for knives, blades, hammer, etc. Non-alloy cold work tool steels shouldn't be used at elevated temperatures (< 200 °C is suggested).

2.2.2 Alloy Cold Work Tool Steels

Compared with non-alloy tool steels, this group of steels has higher hardenability, wear resistance, and average hardness. Regarding the designation of alloy cold work tool steel, we can take X100CrMoV5 as an example. The starting X means at least one element is above 5 wt%. "100" represents the ten thousandths of C. Then, the elements are arranged by their content. The number at the end indicates the percentage of alloying element having the highest amount. The excellent hardenability of this group of steels makes the martensite formation possible by quenching in the medium of oil or air. As a result, the risk of cracking and distortion dramatically decreases. Hence, they are commonly used to produce large dimension parts and the parts demanding minimum distortion. For example, X100CrMoV5 and X153CrMoV12 can be quenched in air because of their high content of Cr. As shown in Figure 1c, the critical cooling rate of X153CrMoV12 is about 0.1 K/s, which is lower than the cooling rate in air (0.3-0.5 K/s). This explains why it can be quenched in air. However, the critical cooling rate of steel 60WCrV8 is about 10 K/s (Figure 2b). So, the quenching for 60WCrV8 needs oil. Not only Cr, but also Mn can improve the hardenability. Steel 70MnMoCr8 with high content of Mn, for instance, can be quenched in air. Alloy cold work tool steels are widely used for cutting tools, woodworking tools, die and forming molds. In some grades, C content is high enough to produce graphite to provide self-lubrication, which will significantly increase the resistance to metal-to-metal wear and galling for the applications such as punches, shears, and arbors.

2.2.3 Alloy Hot Work Tool Steels

The C content in the grades of alloy hot work tool steels varies from 0.25 % to 0.60 %. The advantage of medium C content is not only for a considerable toughness, but also prevention of carbide growth. Stable carbide is a critical feature for hot work tool steels. Other alloying elements, such as Cr (0.80-5.5%), Mo (0-3.2%), V (0.05-2.1%) and W (0-9.5%), are added into these grades to increase the hardenability, making quenching in air possible. More importantly, these elements are strong carbide formers. The formation of a large amount of stable carbides can provide secondary hardening and maintain the microstructure stability when steels are operated at elevated temperatures.

2.2.4 Alloy High-Speed Tool Steels

High-speed steel is generally used to make tools for cutting materials. Due to the high cutting speed achieved, they are named as high-speed tool steels. They are supposed not to lose their hardness even when being used at elevated temperatures. High-speed steel typically contains a high C content (0.73-1.40%). Other typical alloying elements are W, Mo and Co. The first generation of high-speed steel is T1 steel, which contained extremely high W content (around 18 wt.%) and was patented in the early twentieth century. Subsequently, the outbreak of World War II caused a huge demand of low-price high-speed tool steels, which led to the vigorous development of Mo-containing (replacement of W with Mo) tool steel. In general, Cr content in high-speed tool steels is relatively stable (3.5-4.5 wt%). The total content of W and Mo is about 10%. Interestingly, the designation of high-speed steel is different from other tool steels. It starts with HS followed by numbers separated by hyphens indicating the content of alloying elements in the order of W, Mo, V. For instance, HS6-5-2 means this high speed (HS) steel contains 6% W, 5% Mo, 2% V. Usually, high speed tool steels have high hardness (60-67 HRC). A large fraction of stable carbides because of high alloy content is the source of both high hardness and red hardness, which provides an outstanding wear resistance at elevated temperatures.

Owing to high alloy content, the quenching for high speed tool steels usually is performed in the medium of air, gas, or salt bath.

2.3 Heat treatment of Tool Steels

The properties of tool steels are determined by the combination of composition (or grade) and heat treatment. The commonly applied heat treatments are stress relieving, quenching, and tempering. Suitable heat treatment of tool steels should be performed for different application in order to obtain required properties.

2.3.1 Stress relieving

The purpose of stress relieve heat treatment is to remove the internal residual stresses (thermal and mechanical stress). Usually, it is carried out after semi-finish machining before hardening and finish machining. Otherwise it can lead to undesirable dimensional changes. At room temperature, when the residual stress is lower than the yield strength of the material, no distortion occurs. But when the material is heated up to elevated temperatures, the yield strength will decrease and could reach a level lower than the internal stress. As a result, plastic deformation occurs. This is the reason why stress relieving is needed and why it should be performed before hardening and finishing machining steps.

In general, stress relieving is performed at temperatures between 550-700 ℃ for 1-2 hours to make sure the material is heated uniformly, and all the internal stress is relieved. In addition, material should be cooled down slowly to avoid new internal stress formation.

2.3.2 Quenching

The purpose of quenching is to form martensite with high hardness. Austenitizing is utilized to heat the steels and convert the ferrite phase to austenite phase. The austenitizing temperature (sometimes called harden temperature) varies from 780-1250 ℃, which is dependent on the steel's composition and desired properties. The heating should be slow to avoid internal stress. Generally, several degrees per minute is recommended. To make the temperature between the surface and the center of parts uniform, one or two stops at the temperature of 600-650 ℃ or 800-850 ℃ can be set. The holding time is generally recommended to be 0.5 h. Prolonged hold time may result in grain growth. Higher austenitizing temperature is beneficial to the dissolution of C and other alloying elements in austenite phase and to the hardenability, achieving a high hardness in the martensite after subsequent quenching. As shown in Figure 2b, with the increase in hardening temperature, the final hardness after double tempering is increased. This explains why many high alloy tool steels have a high austenitizing temperature (e.g., X30WCrV9-3: 1150 ℃, HS6-5-2: 1220 ℃). However, high hardness is not the only purpose in practical application. Considering low notch toughness and other difficulties caused by coarse grain size resulting from high austenitizing temperature, sometimes, relatively low austenitizing temperature is employed. Another impacting factor is the alloying elements. For some tool steels, ferrite-stabilizing elements (e.g., W, Mo, Cr) in materials will shrink the austenite phase field and increase the austenitizing temperature. On the contrary, austenite-stabilizing elements (e.g., N, Ni, Co, Mn) could extend the austenite phase field on the phase diagram, lowering the critical temperatures, which provides a chance to obtain a finer grain size in the quenched parts.

After austenitizing, a proper cooling rate should be adopted to cool down the steel to the martensite transform start temperature (M_s). High cooling rate may cause distortion or even cracking in the components. Low cooling rate risks the formation of other phases instead of martensite. Hence, a compromise should always be employed. Alloying elements may shift pearlite "nose" to the lower right direction in TTT and CCT diagrams, i.e., the formation of pearlitic or bainitic structure is delayed to

longer times. Therefore, martensite can form even in thick sections at slow cooling rates. Many tool steels contain significant amount of alloying elements to make air quenching possible, or at least easy to quench.

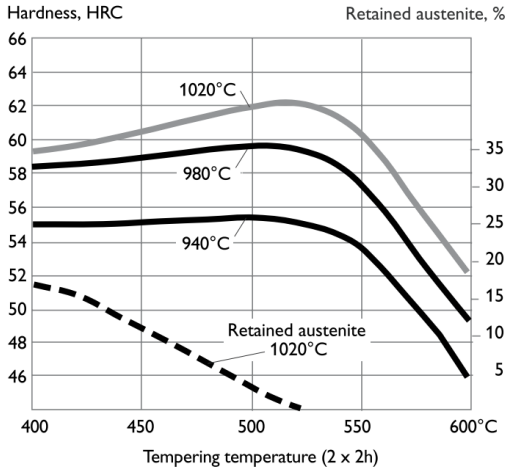

Figure 2. (b) Tempering diagram of V4E cold work tool steel. Adapted from [19].

Also, alloying elements could affect the temperature range of martensite transformation. Most of the alloying elements (except V, Co, Al) lower martensite transformation temperature [19]. This may cause higher internal stress due to the volume increase accompanied by martensite transformation, leading to distortion or even cracks. Meanwhile, lowered martensite transformation finish temperature (M_f) could lead to incomplete martensite transformation and large fraction of retained austenite in quenched parts.

2.3.3 Tempering

The aim of tempering is to improve the toughness of the quenched steels and to reduce or eliminate internal stress. The microstructure tends to stabilize, and tempered martensite is formed. It is suggested that the as-quenched steels should be tempered immediately, because the internal stress in as-quenched parts could cause cracking and fracture of the parts

It is well known that the as-quenched martensite is brittle due to the highly distorted and stressed crystal structure caused by solute carbon atoms in body centered tetragonal structure. After tempering, the stress is relieved, and the carbon diffuses from martensite and forms some fine carbides. This results in an improvement of toughness and there is no distinct decrease of hardness. Another change during tempering is the decomposition of retained austenite to form ferrite and carbides. It should be noted that when the temperature drops to lower than M_s, retained austenite can transform to martensite which is brittle. Therefore, another tempering is necessary to reduce the brittleness. In practice, twice or three times tempering are often performed for many tool steels.

In some high alloyed tool steels, the increase of alloying elements will extend the austenite phase region leading to more stable retained austenite. In this case, a higher tempering temperature (typically > 500 ℃) always employed in order to lower the content of retained austenite (as shown in Figure 2) and therefore obtain a higher hardness and strength. The wear resistance of a steel depends not only on the hardness, but also on the type, size, and amount of carbides. At high tempering temperature, carbides precipitate more efficiently out from martensite and austenite. For some particular carbides, they can only form during tempering at 550 ℃ or higher temperatures.

When selecting the heat treatment parameters, the hardness should never be the only consideration. Same hardness values can be obtained by different types of heat treatment. In some cases, a small amount of retained austenite will improve the fracture toughness distinctly. How to control the proportion of retained austenite and make austenite relatively stable are the key factors. Using a low austenitizing temperature can lead to small amount of retained austenite due to the insufficient dissolution of alloying elements during austenitizing. This not only ensures that the hardness will not drop significantly, but also improves the toughness of the steels. Then, double tempering the steels at low temperature (may be 180-250 ℃) can make the retained austenite relatively stable for the further application. This strategy can be used on some cold work tool steels.

Chapter 3 – Additive Manufacturing

Additive manufacturing (AM) technology has been developed over the past 30 years. It started as a technology for rapid prototyping. The early period of AM mainly focused on non-loading materials, such as polymer, ceramic. The metallic AM is a newly developed field, which inherited the advantage of free designing. With this characteristic, metallic AM could produce parts with complex shapes and functional gradients which is nearly unlikely by traditional methods. Today, the metallic AM technology is mainly applied in automotive, biological implants, aerospace and in other fields with specific requirements [20]. Compared to conventional parts, metallurgical differences lead to some challenges (e.g., excessive residual stress, microstructural anisotropy, and common defects) for AM parts, limiting the application of AM components in various fields [20]. While AM technology can be widely used in applications with high tolerance for surface roughness such as surface hardening, medical implants, other demanding parts with high performance such as turbine blades are at an earlier stage of development and need substantial post processing.

Significant progress has been achieved over the past twenty years in the metallic AM technology considering maturity laser technology, reliable powder feedstock system and high-performance computing hardware and software. In terms of materials and metallurgy, the research has been focused on a better understanding of the relationship between powder materials, processing parameters, microstructures, and properties, aiming at defect-free, structurally reliable AM metallic parts.

The widely used AM processes can be classified into two categories: powder bed fusion (PBF) and directed energy deposition (DED). The heat source for AM includes laser beam (L), electron beam (EB), gas metal arc (GMA) and plasma arc (PA). The abbreviation of heat source is often added in the designation of an AM process. Some examples are L-DED, EB-DED, GMA-DED, LB-PBF, and EB-PBF. The three main processes are LB-PBF, EB-PBF and L-DED.

3.1 Laser Beam Powder Bed Fusion (LB-PBF)

LB-PBF is a process to create a three-dimensional object layer by layer using laser beam (Figure 3) from computer aided design (CAD). A CAD file contains the information of the part produced and its support structures, which are sliced into numerous thin layers. Also, a variety of processing parameters (e.g., scanning path, thickness of layers, hatching space, etc.) are set in the CAD files [21-24]. The parts are built by spreading powder layers and melting selective regions, layer by layer within a

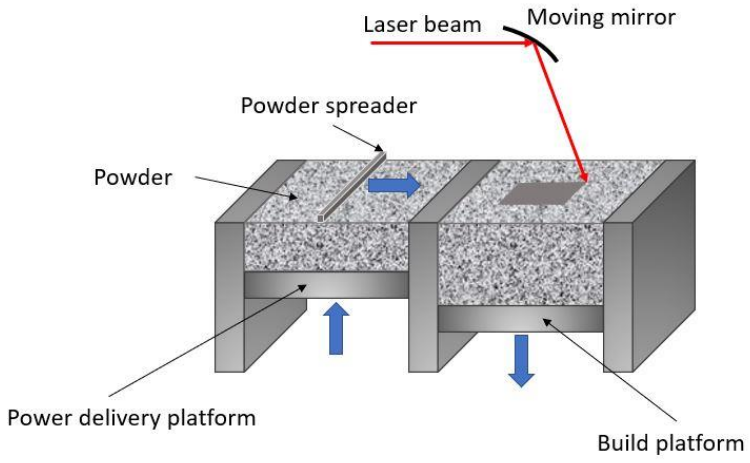

Figure 3. Schematic diagram of LB-PBF.

chamber filled by inert gas. The laser beam manipulated by a galvanometer driven mirror reacts with the metal powders resulting in melting tracks which solidify rapidly. The mechanism of EB-PBF is similar to LB-PBF but the heat source is EB instead. EB-PBF allows faster scanning speed but raw powder is limited to electrically conductive materials.

3.1.1 Feedstock Material

It is generally believed that the quality of built parts is greatly influenced by the characteristics of alloy powders used in LB-PBF. The relationships between powder characteristics (e.g., particle morphology, size distribution, chemical composition) and the resulting part properties has been discussed in many publications [25-27]. In the reference of [28], when decreasing the powder size of 316L stainless steel in LB-PBF, the powder packing density will increase, which leads to a higher part density and surface quality. On the contrary, shifting the powder size distribution to coarser direction, the printed parts had a higher elongation at fracture [29]. The size distribution of powders can be measured by sieving or laser diffraction methods. It is not always a positive correlation between characteristics of power and the quality of parts. Lutter et al.[31] reported that even with a highest powder packing density by adjusting powders size distribution, the density of final parts is just relatively modest.

The qualities of powders largely depend on the way of manufacturing. Normally, the powders produced by plasma atomization and gas atomization are popular because of a good sphericity and lower porosity. Despite the nearly perfect quality of powder from plasma atomization, the high cost and low yield make it less attractive from economic point of view. The powder produced by water atomization is also used in some cases. However, the irregular shape and worse size distribution worsen the surface quality of the parts produced [30].

One advantage of AM technology is the optimized usage of raw materials which is meaningful considering limited resources on our planet. Typically, the powders utilized in AM building process is just a small fraction and rest of the powder will be recycled. In industrial AM practice, the powders may be reused for more than a few tens of times. However, the reused powders deteriorate even in vacuum or inert gases environment. Aggravated oxidation, agglomeration of powders and the change of chemical state of powder surface may occur. For instance, the thickness of oxide layer on used copper powders is greatly dependent on the purity of the powder. Higher purity could lead to a relative thin oxide layer [32]. Surface roughening, particle sintering, and elements evaporation were found on the reused Ti-6Al- 4V powders after EB-PBF process [33]. The quality of reused powder should be considered because it will influence the properties of built components, especially for oxygen sensitive materials such as Titanium alloys. To summarize, the correlation between powder characteristics and printed parts is complex.

3.1.2 Process parameters

There are many parameters in an AM process, such as laser power, layer thickness, scanning velocity and hatching space etc. that influence the microstructures and properties of the printed part. Also, these parameters interact with each other. The influence of some parameters is discussed in the following text.

Laser power. Power is a critical parameter, which will significantly impact the melt pool size, penetration depth, defects, cooling rate, evaporation of alloy elements and so on. With a higher power, the size of melt pool will increase because of larger heat input. The benefit is the sufficient melting of the powder, leading to dramatically reduced lack of fusion and consequently increased the density of the builds. The cooling rate is also affected by power level. Higher power will decrease the cooling rate and consequently the thermal stress during the solidification, minimizing the tendency of cracking. On

the other hand, too high power should be avoided, because it increases temperature of melt pool, accelerating the vaporization of alloying elements. Meanwhile, the recoil pressure caused by vaporization could eject the molten droplets from melt pool [34-35].

Power is not the only factor that determines the heat absorbed in a melt pool. Power density distribution and energy absorption coefficient are also important characteristics of heat source. Generally, the power density distribution P_d of a laser beam follows the Gaussian profile, which can be expressed as Equation (1) [36]:

$$P_d = \frac{fP}{\pi r_b^2} exp\left(-f\frac{r^2}{r_b^2}\right) \quad (1)$$

where P is the function of laser power, f distribution factor and r radial distance from the beam center. When taking the absorption coefficient into consideration, the expression of $P_d$will change to Equation (2) [37]:

$$P_d = \frac{fP}{\pi r_b^2 t_l}[\eta_P + (1-\eta_P)\eta_l] exp\left(-f\frac{r^2}{r_b^2}\right) \quad (2)$$

Where η_P is the fraction of energy absorbed by the powder during interaction, η_l is the absorption coefficients of the deposit, and t_l is the layer thickness.

Scanning speed. Generally, scanning speed is coupled with the power of heat source. For a fixed heat input, scanning speed is inversely proportional to the power. Increasing the scanning speed will decrease the volumetric energy density (VED), which can be defined in Equation (3):

$$VED = \frac{P}{v*h*t} \quad (3)$$

Where v is the scanning speed and t refers to layer thickness. It is seen from Equation (3) that the melt pool will be elongated, narrow and shallow at condition of constant VED and higher scanning speed. Continue to increase the scan speed will increase the trend of lack of fusion, similar as decreasing power. This is accompanied by high cooling rate, which will increase the susceptibility of cracking. Although high scanning speed increases the yields of printed parts, a compromise should be made for ensuring the quality.

Scan strategy.

During the process of LB-PBF, laser scanning strategy influences the thermo-mechanical behavior of parts. Thermal gradients created by the temperature fields using different scanning strategy in LB-PBF lead to residual stresses, which could cause distortion and cracking in the printed parts. The frequently used strategies are unidirectional, bi-directional (or named as zigzag path), island and contouring out-in (in-out) scanning. In reference [38], a simulation of temperature and thermal gradient was performed, as present in Figure 4. In the zigzag strategy, overheating is found in the start region of each track because this start region has been preheated by the end of previous track. Similar interpretation applies to the temperature field distribution in the next two strategies. The thermal gradient, which has an opposite tendency compared to temperature, are also shown in Figure 4 d, e, and f. Decreasing the thermal gradient contributes to reduced thermal stresses.

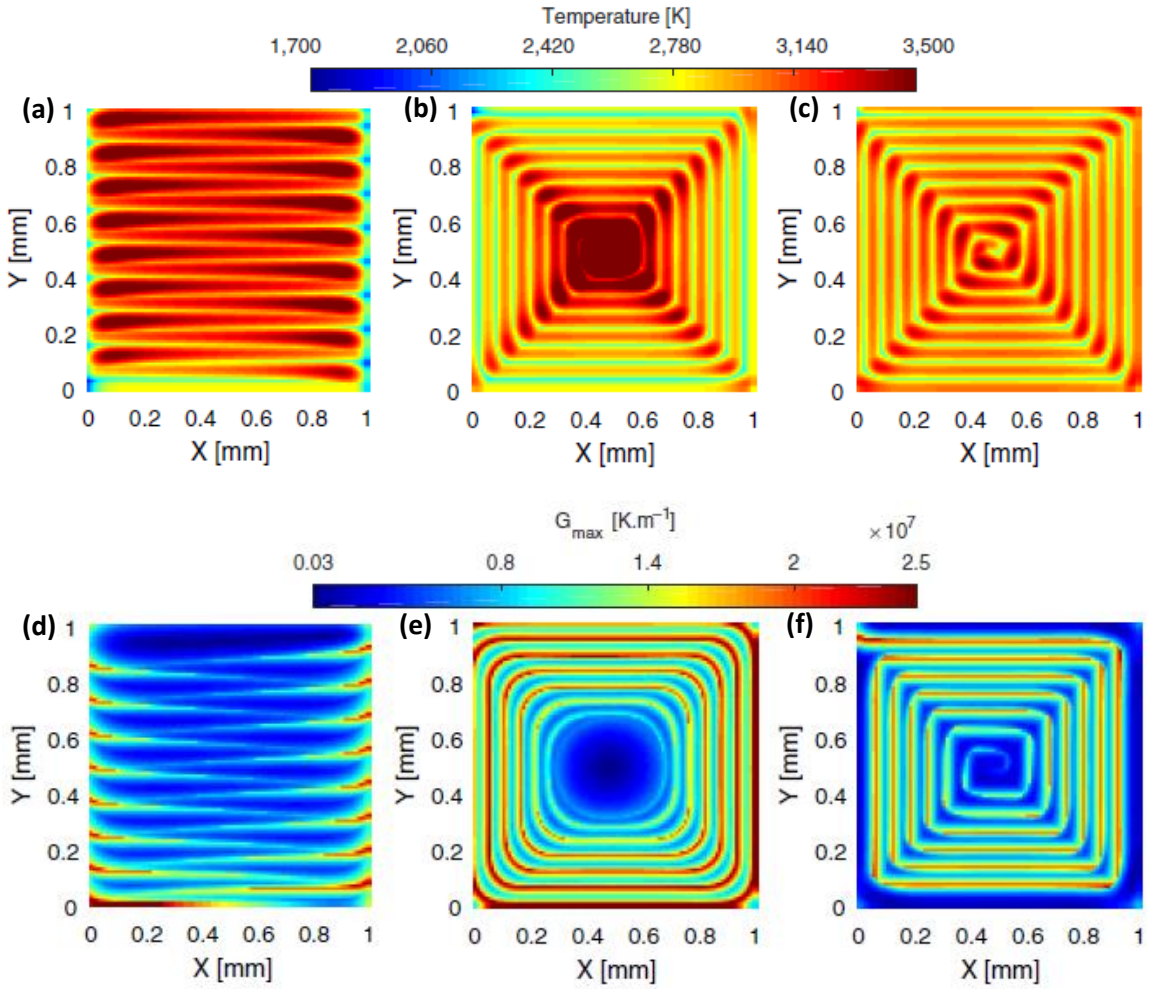

Figure 4 The simulated results of temperature and its gradient using different scanning strategies: (a)&(d) the zigzag path; (b)&(e) outside to inside path; (c)&(f) inside to outside path (Image reproduced with the permission of Emerald [38]).

To obtain high density parts, many other aspects should also be taken into consideration, such as processing atmosphere, preheating, and powder layer thickness. Three critical indices related to the melt pool dimension (melt pool depth D, width W, and length L) are the ratio of depth-to-layer thickness (D/t), width-to-hatching space (W/h), and length-to- width (L/W) [39]. It has been reported that relative high density is generally obtained in the index range of $1.5 < D/t < 2$, $1.5 < W/h < 2.5$ and $L/W < 2\pi$ [40-41]. The process parameters are material dependent and needs further exploration.

3.2 Directed Energy Deposition (DED)

L-DED, also called laser cladding, is a process in which metal powder/wire from a nozzle is fused onto a metal surface by the focused beam of a high-power laser in a protective atmosphere. In this thesis, feedstock material is metallic powders and the heating source is laser beam. DED refers to metal powder directed energy deposition by laser beam in the following text. The schematic diagram of such DED process is shown in Figure 5. Powder is delivered in a coaxial way with laser beam and protected by shielding gas such as argon. Similar to most of the AM processes, a CAD file is used to guide the fabrication of components. The overhanging features in the part may require supporting structure to avoid distortion caused by heat and their own weight [42]. The processing parameters such as scanning speed of the laser beam and the feed rate of the powder are either pre-set or adjusted in the process.

DED technology is often used to produce components with rough blank shapes requiring post machining to achieve the desired geometry and surface quality.

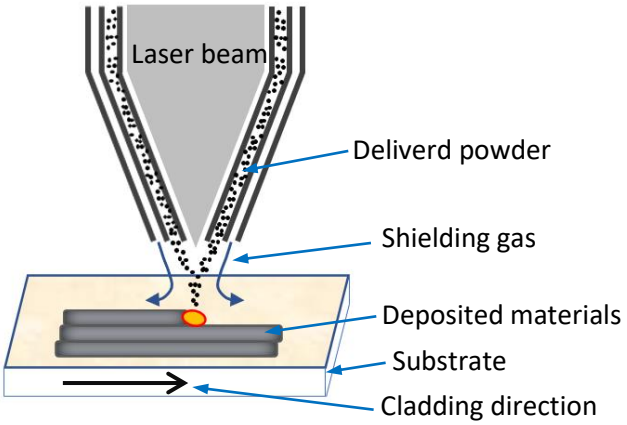

Figure 5 Schematic of directed energy deposition.

3.2.1 The comparison of L-DED versus LB-PBF

Forming a melt pool using laser beam is the fundamental for both DED and LB-PBF technology. Theoretically, they have the similar mechanism compared to that of welding. However, many differences exist between DED and LB-PBF. Table 1 presents a comparison of L-DED and LB-PBF technology. In most cases, DED has a higher laser power than that of LB-PBF, making the melt pool in DED is larger than in LB-PBF. Consequently, the dimensional accuracy of DED is not as good as LB-PBF [36]. Nevertheless, the laser power is a major factor that influences the building efficiency. Larger melt pool will increase the building efficiency if the powder feed rate is increase correspondingly. Compared to LB-PBF, DED technology is more convenient to manufacture larger dies and repair/refurbishment of production dies because of its freedom of material deposition. It is also more effective when developing functionally graded materials.

Both DED and LB-PBF are available to manufacture parts with complex shape that are difficult to machine or build by conventional methods. The selection of AM technique is dependent on the dimensional tolerance, build size, mechanical properties and the acceptance level of defects. Considering the opportunity offered by these techniques, in-depth knowledge regarding processing, microstructure and properties is of great importance for tool steels.

Table 1. Comparison of main features of directed energy deposition by laser beam (L-DED) and laser powder bed fusion (LB-PBF) [36].

Process	L-DED	LB-PBF
Heat source	Laser	Laser
Powder delivering type	Coaxial delivering	Pre-spread powder layer
Power (W)	100-3000	50-1000
Speed (mm/s)	5-20	10-1000
Max. build size (mm*mm*mm)	2000*1500*750	500*280*320
Dimensional accuracy (mm)	0.5-1.0	0.04-0.2
Surface roughness	4-10	7-20
Post processing	HIP and surface grinding are seldom required	HIP is rarely required

3.3 Microstructure and Properties of Tool Steels Fabricated by AM

3.3.1 Solidification and microstructure

Solidification and microstructure of the parts fabricated by AM process are often affected by many processing parameters. Temperature gradient G (K/mm) and growth rate R (mm/s) are the most important physical quantities in solidification, which determine the morphology and size of microstructure in the as-build state. Figure 6 shows the influence of G/R and G×R on the solidification microstructure. With decreasing the ratio (G/R) of thermal gradient and growth rate, the morphology will change in the sequence of planar → cellular → columnar dendrite → equiaxed dendrite. On the other hand, the higher G×R value (essentially this is the cooling rate) will lead to a finer structure. The cooling rate in AM process is generally higher than that in the traditional casting. Usually, it is in the range of 10^3 -10^5 K/s for DED and 10^5 -10^7 K/s for LB-PBF, respectively. Consequently, the microstructure in AM metal parts is finer than that in traditional ones. Due to the difference of the cooling rate in DED and LB-PBF, the morphology in LB-PBF is usually cellular, which is different from the columnar dendrite or mixture of cellular and columnar dendrite.

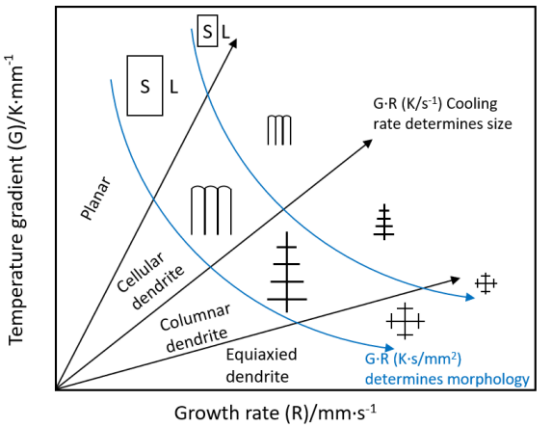

Figure 6. The influence of temperature gradient and growth rate on the morphology of solidification microstructure. Adapted from [8].

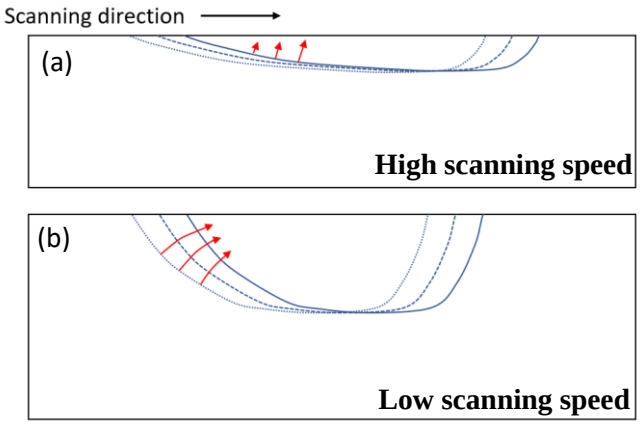

Figure 7. Schematic illustration of the direction of grain growth under different scanning speed. (a) high scanning speed, (b) low scanning speed. Adapted from [36].

During solidification, grains in metal tends to grow along the heat flow direction which is usually perpendicular to the melt pool boundary. However, this direction is different in LB-PBF and DED. The melt pool in LB-PBF is a long and shallow due to its high scanning speed. This geometry will lead to a

nearly vertical growth of the grains, i.e., roughly along the building direction, as indicated by the arrows in Figure 7a. Relatively larger power and smaller scanning speed make the melt pool in DED deeper compared to that in LB-PBF, as shown schematically in Figure 7b. The grains may grow deviating from the building direction due to local curvature of the solid/liquid interface as indicated by the arrow in Figure 7b. Consequently, the grain orientations in the component fabricated by DED usually have a relative larger angle with respect to the building direction. Another phenomenon is the "competitive" grain growth. At the early stage of solidification, extensive grains with different orientations are nucleated due to the large nucleation rate. Only the grains with the orientation parallel to heat flow direction have high chance to survive.

3.3.2 Mechanical Properties

High cooling rate leads to a fine microstructure. AM parts are thus expected to have excellent mechanical properties. In fact, AM parts after post heat treatment do have a comparable or even higher strength than conventional parts often at the expense of ductility. The high strengths are usually attributed to the fine grain features due to rapid solidification. In addition, the potentially high dislocation density caused by rapid solidification and residual stresses contribute as well. The low elongation in AM metal parts originates from the combined effect of high dislocation density, internal defects such as sharp lack-of-fusion or uneven microstructure between the boundary and center of melt pool [43]. Processing parameters also affects mechanical properties. Lower volumetric energy density results in a smaller melt pool, faster cooling rates and finer structures compared to the parts fabricated with higher volumetric energy density. This will lead to higher yield and ultimate tensile strength in the materials.

Since tool steels are the target material of this thesis, the discussion here will focus on the mechanical properties of AM tool steel including hot work tool steels, cold work tool steels and high-speed tool steels. H13 hot work tool steel is extensively studied among these tool steels. The typical mechanical properties reported for AM H13 are shown in Table 2. The hardness ranges from 530 HV to 670 HV in LB-PBF parts, which is comparable or even higher than wrought H13. This means the as-printed parts have a microstructure with less retained austenite due to the intrinsic tempering by the neighbor layers. The yield strength and UTS of the as-built parts are usually lower than wrought one owing to the brittle marteniste. After tempering, the strengths have a significant improvement and are close to the wrought materials. Another issue is that the elongation of as-built LB-PBF parts is much lower. It suggests that the microstructure with a high fraction of martensite in the LB-PBF produced H13 is brittle and needs further heat treatment. In the case of DED, the hardness has a range of 460 HV to 660 HV. It is hard to prepare tensile specimens due to the limited thickness, so only limited data of tensile properties of DED H13 is available in literatures. According to [49], the yield strength and UTS of DED H13 material is close to wrought one. The elongation (5-6 %) in these parts needs distinct improvement. In addition, it presents an even better wear resistance than conventional counterparts in pin-on-disc test. Compared to LB-PBF, it seems the mechanical properties of H13 parts made by DED are promising.

Usually retained austenite is observed in as-printed AM parts in many tool steels such as cold work tool steels X65MoCrWV3-2 [55] and high-speed steels M2 [56-57] and M3.2 [58] due to their high content of C and other alloy elements. Hence, the hardness of these AM materials in as-printed state is probably lower than conventional materials. For instance, cold work tool steel D2 produced by DED has a hardness of 43-45 HRC [53], which is significantly lower than that of wrought D2 (58 HRC) [54]. In addition, a higher hardness is obtained at the bottom layers than the top layers due to the intrinsic tempering during the process. Figure 8 shows the hardness profile of V4E cold work tool steel fabricated

by DED. It can be seen that the top layer has a hardness of 710 HV, which is lower than the hardness from the layers below due to lack of intrinsic tempering. After a double tempering for 3h at 550 ℃, the hardness can reach values as high as ~920 HV once retained austenite is removed.

Table 2 Overview of mechanical properties of AM H13 steel. AP: as-printed, AH: age hardened (tempered), PH: pre-heated baseplate.

Condition	YS (MPa)	UTS (MPa)	δ (%)	Hardness	Ref.
H13 wrought AH	1569-1650	1930-1990	9-12	40-53 HRC.	[44-45, 49]
LB-PBF AP		1000-1200	0.8-1.9	612 HV	[46]
LB-PBF AP	1150-1275	1550-1650	1.5-2.25		[47]
LB-PBF AP	1236	1712	4.1		[45]
LB-PBF AP (PH: 200 ℃)	835	1620	4.1		
LB-PBF AP (PH: 400 ℃)	1073	1965	3.7		
LB-PBF AP	1003	1370	1.7	59 HRC	[44]
LB-PBF AH	1580	1860	2.2	51 HRC	
LB-PBF AP (PH: 240 ℃)	892	1440	1.5	571-579 HV	[48]
DED AP	1288-1564	2033-2064	5-6	660 HV	[49]
DED AP				46-54 HRC	[50]
DED AP				550 HV	[51]
DED AP				400-600 HV	[52]
DED AP				53-56 HV	[53]

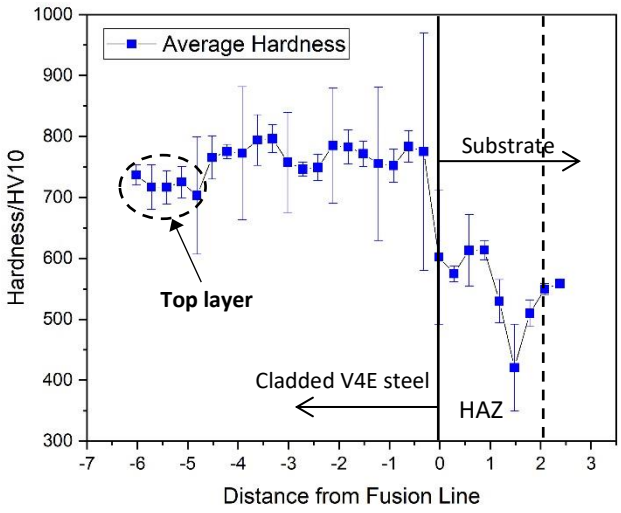

Figure 8. Hardness profile of V4E cold work tool steel produced by DED. HAZ is heat affected zone of substrate.

3.4 Defects in AM parts

Defects are a common topic in AM field. Cracks and voids are the major defects of concern in AM parts. Before focusing on these two types of defects surface roughness and element evaporation will be discussed first.

3.4.1 Surface roughness and element evaporation

The evolution of surface roughness is a complex phenomenon. It could be caused by both the intrinsic fluctuation of melt pool shape and the balling or partially melted particles on surface. It is related to

melt pool size, powder particle size and processing parameters[59-60]. Kempen [57] reported that remelting is an effective way to improve the surface quality (seen Figure 9). Indeed, it can improve both the relative density and surface quality of LB-PBF fabricated M2 steel. The arithmetic mean surface roughness can decrease to a value of 8.6 μm from 18.3 μm. Meanwhile, the porosity and particles on surface were extensively eliminated.

Element evaporation, also referred as loss of alloying elements, takes place during AM process when the melt pool temperature is high. The consequence is the changes in composition which will affect the solidification microstructure and mechanical properties [61]. Therefore, it can be a serious issue for the high-quality demanding parts. Usually, the vapor flux is proportional to the equilibrium vapor pressure, which is strongly dependent on temperature, especially at higher temperatures. The selection of processing parameters, such as higher power, lower scanning peed, can increase melt pool temperature which will increase the vapor flux. However, a "counterintuitive" finding was reported [62] that a higher aluminum content was obtained at the "slow and hot" condition during the DED process of Ti-6Al-4V. It is explained that a lower surface to volume ratio in a bigger melt pool leads to less compositional variation.

3.4.2 Porosity

Porosity is a common defect in AM parts that should be avoided as much as possible due to its detrimental effect on mechanical properties. Generally, porosity in AM parts can be categorized into three type: lack of fusion, voids from keyhole and trapped gas pores.

Lack of fusion porosity is caused by the insufficient melting and consequently incomplete adherence to the previous layer or track. It is related to the ratio of melt pool depth to layer thickness, which can be used as an index of lack of fusion [61]. The voids of lack of fusion often present an irregular shape at the lower position of melt pools. Adjusting the processing parameters that increase the melt pool depth or decrease the layer thickness can minimize the tendency of lack of fusion. It has been experimentally proved that higher heat input by increasing laser power or decreasing scanning speed can effectively reduce or even eliminate the porosity caused by lack of fusion [61, 63-64]. Additionally, adjusting hatch spacing to obtain a proper bonding to previous track is also an effective way to reduce lack of fusion [65]. In some cases, the voids in melt just have inadequate time to float up to melt pool surface. Therefore, the liquid surface tension and viscosity of an alloy are important factors as well. Moreover, melting temperature and thermal conductivity, which could influence the dwell time of melt pool, also affects the formation of lack of fusion.

Keyhole porosity originates from the tip of keyhole. Essentially, keyhole is not a type of defect. It's formed in the liquid melt pool when the strong recoil pressure from the rapid evaporation of the metal pushes the surrounding molten liquid downward, as shown in Figure 9 [66-67]. During the high-power density melting, the shape of keyhole will become narrow and deep and the tip will be instable. Without proper control, the tip could collapse from keyhole and be trapped by the solidification. The size of keyhole porosity depends on the size and shape of keyhole.

Trapped gas pores could be from either powder particles or trapped shielding gas in melt pool. The pores usually present a spherical shape. In laser AM techniques, inert gas such as argon and helium are often employed as shielding gas. Usually, these gases are insoluble in metal liquid and don't react with metal liquid [68]. If trapped into liquid, inert gas either floats out of melt pool or is left inside solid after solidification. However, it will not change the composition of molten alloy. When using nitrogen as shielding gas, situation is different because nitrogen can dissolve into metal liquid before floating out

or being trapped by solidification. How this affects the properties is material related. For LB-PBF 316L stainless steel, only limited differences are shown when comparing nitrogen and argon [69]. But for some metal such as Ti-6Al-4V, nitrogen shielding gas could react with liquid metal and leads to deterioration of properties [69].

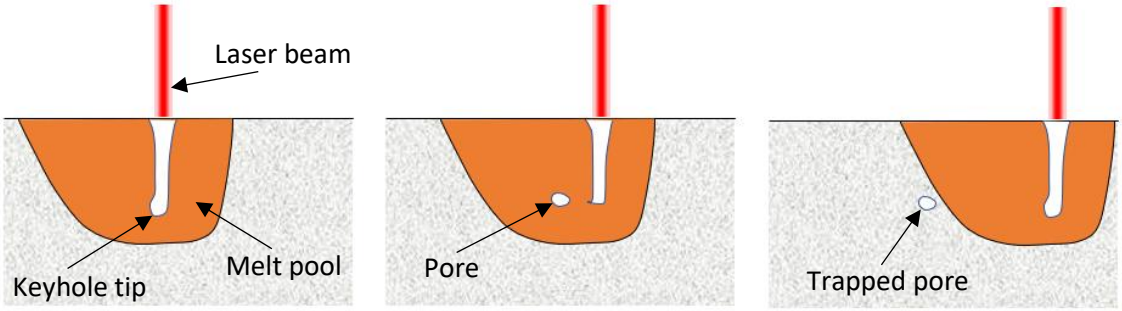

Figure 9. Keyhole porosity formation from the instable keyhole tip. Reproduced from [67].

3.4.3 Cracking

Cracking in AM parts includes delamination and hot cracking. In this thesis, we focus on hot cracking, also known as solidification cracking, which is caused by uneven contraction during solidification. In an AM process, the temperature of the new built layer is higher than that of the previous layer (or substrate). Hence, the contraction caused by cooling in the new layer is more than that in previous layer, which will lead to a tensile stress in the new layer. If the tensile stress is high enough, hot cracking will initiate at weak places. This tensile stress caused by temperature change is named as thermal stress (σ). It is determined by three factors[70]: temperature change (ΔT), elasticity modulus (E) and thermal expansion coefficient (α), as given in Equation (4):

$$\sigma = E\,\alpha\,(T_f - T_o) = E\,\alpha\,\Delta T \tag{4}$$

where T_f, T_o represent final and initial temperature of solid respectively. It is seen from Equation (4) that materials with a high thermal expansion coefficient α will have a relatively high thermal stress σ during the cooling process. To avoid cracking, the thermal stress should be minimized, and the threshold strength of tearing should be increased. There are two basic routes including composition control and processing parameter tuning. The former one focuses on metallurgical factors to reduce the temperature range of solidification, especially the temperature range of the last stage of solidification.

Regarding compositional aspect, a cracking criterion was proposed by Kou [71]. It is based on the maximum slope of $|dT/df_s^{1/2}|$ in the last stage of solidification, which corresponds to solid fraction f_s of 0.95, for instance. The term of $|dT/df_s^{1/2}|$ is the susceptibility of cracking and can be expressed as in Equation (5) [71]:

$$\left|\frac{dT}{df_s^{1/2}}\right| = \frac{2(1-k)(T_m-T_E)\sqrt{1-f_E}}{f_E} \tag{5}$$

where k is partition coefficient, T_m is the melting temperature of solvent, T_E is the eutectic temperature, f_E is the faction of eutectic structure. Figure 10 compares the predicted hot cracking susceptibility by Equation (5) and experimental crack density of Al-Si binary alloy. Two curves show almost the same tendency except the difference of Si concentration for the highest susceptibility. In order to solve this problem, Liu and Kou [72] suggested that the effect of solid-state diffusion should be taken into

consideration. An additional dimensionless parameter α including the effect of diffusion is employed, which is expressed as Equation (6) [72]:

$$\alpha = \frac{4D_s t_f}{\lambda_2^2} \tag{6}$$

Where D_s is the diffusion coefficient of the solute in solid matrix, t_f is freezing time, λ_2 is the secondary dendrite arm spacing. Then, f_s can be expressed as Equation (7), where T is the temperature of melt, C_0 is the concentration of solute, and m_L is the slope of the liquidus [72]:

$$f_s = \frac{1}{1-2\alpha' k}\left[1 - \left(\frac{T_m - T}{-m_L C_0}\right)^{\frac{1-2\alpha' k}{k-1}}\right] \tag{7}$$

where α' is expressed as:

$$\alpha' = \alpha\left[1 - \exp\left(-\frac{1}{\alpha}\right)\right] - \frac{1}{2}\exp\left(-\frac{1}{2\alpha}\right) \tag{8}$$

Adopted from [73], D_s is chosen from 2×10^{-9} to 9×10^{-9} m^2/s, which is consistent with the self-diffusion coefficients at right below the melting temperature and the predicted result is consistent with the experimental results.

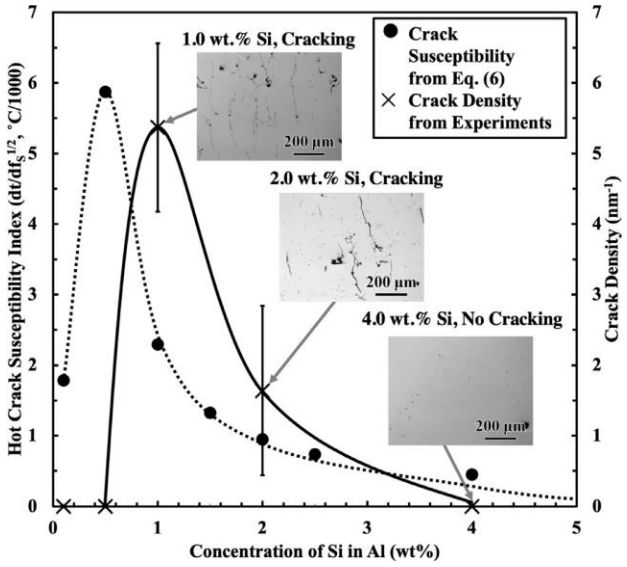

Figure 10. Hot cracking susceptibility prediction vs. measured crack density for binary Al-Si compositions examined (Reproduced with the permission of Elsevier [73]).

In most cases, the composition of an alloy is fixed. Therefore, tuning the processing parameters is a good way to avoid cracking. According to Equation (4), increasing the final temperature of the component can decrease the temperature change during the cooling process, which can reduce the thermal stress proportionately. Preheating the baseplate is an effective way to avoid hot cracking [14]. High preheating temperature above the martensite start temperature M_s will prevent the martensite transition [75] and leads to transformation of austenite to upper bainite [76]. Preheating can also decrease the thermal gradient G and the cooling rate. Hence, the dimensionless parameter α in Equation (6) will increase accordingly, which will help to decrease the hot cracking susceptibility.

It is believed that the fine and isotropic microstructure is beneficial for high tearing resistance. Epitaxial growth and the coarse columnar dendrites are undesirable. Obviously, high cooling rate can help to

obtain a fine structure. Another way is to use nucleating agents which increases nucleation rate during solidification in an AM process, leading to a fine microstructure. Martin et al [77] incorporated TiC nanoparticles into 7075 and 6061 series Al alloy powders during the LB-PBF. A crack-free, fine-grained microstructure was obtained. The final strengths are comparable to wrought materials. However, it is not easy to find a suitable nucleating agent because it should match the crystallographic lattice spacing and density to provide a low-energy nucleation barrier according to classical nucleation theory.

Chapter 4 - Experimental Methods

4.1 Materials and sample preparation

4.1.1 Modified H13 hot working tool steel

The nominal composition of the alloy is X32CrMoV3-2. It was modified on the basis of H13 tool steel (M-H13) to optimize the properties at elevated temperatures for the intended applications. In this study, parts were produced by LB-PBF using gas atomized powders supplied by Uddeholms AB. The particle size of the powders is in the range of 20 μm to 50 μm. For the microstructure characterization, samples were prepared by following standard Struers metallographic procedure and then etched with the etchant of 5% picric acid + 1% HCl + 94% ethanol for 30 seconds.

4.1.2 Vanadis 4 Extra SuperClean

Pre-alloyed Vanadis 4 Extra SuperClean (V4E) cold work tool steel powders, gas atomized and supplied by Uddeholms AB were used as feedstock material of DED processing. The chemical composition is shown in Table 3. The substrate is made by Dievar hot work tool steel in the size of 117 × 59 × 25 mm^3, supplied by Uddeholms AB as well. The V4E powders in the particle size between 45 μm to 150 μm were cladded on the substrate in the form of 1-layer, 2-layers, and 4-layers. For the microstructure characterization, samples were etched with of 5% picric acid + 1% HCl + 94% ethanol for 30 seconds.

Table 3. Chemical composition of V4E steel and Dievar steel provided by the powder suppliers.

	C	Si	Mn	Cr	Mo	V	Fe
V4E	1.4	0.4	0.4	4.7	3.5	3.7	Bal.
Dievar	0.35	0.2	0.5	5	2.3	0.6	Bal.

4.1.3 LB-PBF system

Cubes of M-H13 steel in the size of 10 × 10 × 10 mm^3 were produced by LB-PBF method using SLM 125 HL system (SLM solutions Group AG) equipped with a YAG laser of maximum power of 400 W. The laser has a power of 175 W and a beam diameter of 65 μm. The building chamber was filled with inert argon gas (12 mbar inside pressure). The preheating temperature of baseplate was 200 ℃. The scanning speed is 720 mm/s and hatch spacing between tracks was about 120 μm. The layer thickness was chosen to be 30 μm.

4.1.4 DED process

For the V4E powders, they were cladded on the Dievar substrate by DED method. The DED system is combined with a 5-axis DED Laser printing machine with a YAG laser of maximal power of 4000 W. The laser power applied in this study is 1600 W. The shielding gas used to carry powder and protect melt pool was argon inert gas. Before the cladding, the baseplate wasn't preheated. The scanning speed is 520 mm/min and the hatch spacing between tracks was 1.8 mm. The layer thickness was designated to 1.6 mm. Zigzag scanning pattern was applied in cladding process. For the 1-layer and 2-layers specimen, the cladding area is 102 × 52 mm^2, and for the 4-layers specimen, the cladding area was changed to 48 × 50 mm^2.

4.1.5 Post Heat Treatment

After LB-PBF, selected M-H13 steel samples were divided into two groups. The samples in the first group were treated at 1020 ℃ for 30 min followed by quenching in oil and subsequently tempering twice at 580 ℃ for 2 h. The samples in the second group were directly tempered at 625 ℃ for 2 h to

reduce the retained austenite and for the stress relief. Selected samples from these two groups were treated at 550 ℃ and 600 ℃ for 5 - 100 h followed by air cooling to evaluate the softening behavior at elevated temperatures.

4.2 Analysis Techniques

4.2.1 Optical Microscopy

A Leitz DM-RZ light optical microscope (OM) with Axiovision 4.8 software and a Zeiss Axioscope 7 light optical microscope with Zen Core 2.7 software were used for imaging the microstructure on polished and etched sample surfaces. Integration function provided by Zen Core 2.7 software was used to stitch the images to obtain a large field of view. Subsequently, the relative density of samples was measured using ImageJ software. As shown in Figure 11, the region of the cladded layer is first extracted from the overview image on the cross section (Figure 11a). Subsequently it was converted into 8-bit grayscale (Figure11b) in order to separate the feature with different contrast. Adjusting the upper and lower threshold properly can highlight the edge of the features of interest which is defects in this case (Figure11c). Last, the thresholded pixels were set to black and all other pixels to white (Figure 11d), by which the area fraction of the defects in this image can be measured and relative density can be estimated. Notice non-porosity defects (e.g. cracks) were included. The relative density value is averaged from 8 stitched images.

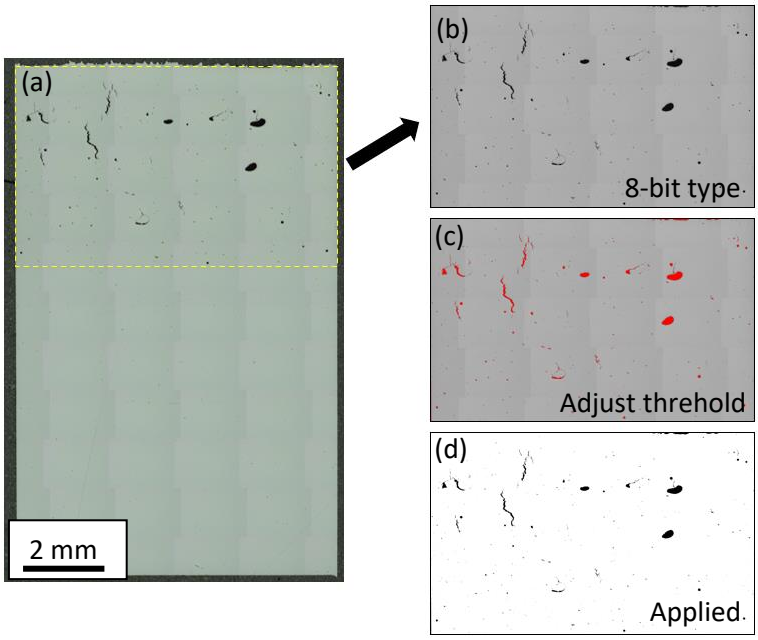

Figure 11. The process of measuring relative density of V4E cladded layer from OM images using ImageJ software.

4.2.2 X-ray diffraction

If monochromatic X-rays is radiated at a crystalline material, one observes diffraction of X-rays at various angles. X-rays generated from a given anode material have a constant wavelength. The commonly used anode materials are Cu and Cr. The relationship between the X-ray wavelength, λ, the angle of diffraction, 2θ, and interplanar spacing of the crystal lattice, d, is given by Bragg's law in Eq.9.

$$n\lambda = 2d\sin\theta \tag{9}$$

where n represents the order of diffraction. The diffraction can occur only for some specific interplanar spacing. In a Bragg-Brentano geometry, the incident angle is varying simultaneously. The primary phases in metallic sample can be identified by X-ray diffraction (XRD) through analyzing their lattice structure. In present study, Bruker AXS D8 Advance diffractometer equipped with Cr K_α radiation is used. Prior to the measurement, the samples were ground and polished following the standard Struers metallographic procedure.

4.2.3 Scanning electron microscopy

Scanning electron microscopy (SEM) is a versatile equipment as it can provide various information depending on the user's demand. As its name implies, an electron beam is used to scan the specimen surface. Various types of signals are generated when the electron beam is interacting with the specimen, such as secondary electrons (SEs), backscattered electrons (BSEs) and auger elections. These signals are subsequently detected by appropriate detectors. Making a good use of these signals can result in highly useful information about the specimen materials.

For example, SEs originated from the atoms at the near-surface regions of the specimen, can give the topographic information of specimen's surface. SEs are a result of inelastic interaction between primary electron beam and the specimen's surface atoms. The interaction volume of SEs is relative smaller compared to BSEs and X-rays, as shown in Figure 12. Although the interaction depth of electron beam and specimen can reach a magnitude of micrometers, only the electrons originating from a depth less than 10 nm can escape and be captured by detector [79]. This shallow depth of SEs makes them suitable for depicting the topography. SEM in this mode usually has high resolution, typically ~10 nm.

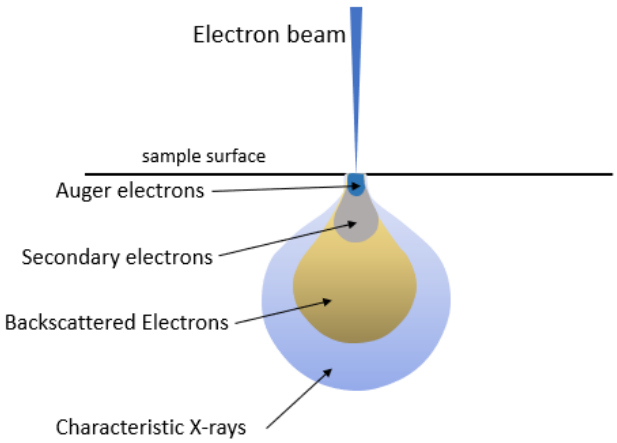

Figure 12. Schematic of electron beam interaction.

Different from SEs, BSEs essentially are the primary electrons. They are from elastic scatter between sample's atoms and electron beam. After interaction, there is no loss of energy compared to primary electron. With a higher energy, the generation volume of BSEs is larger than that of SEs, about several tens of nm. Hence, the mode of BSEs can also give the information of topography but has a poorer resolution than SEs. During the scattering, larger atoms have a stronger ability of scattering electrons than light atoms. Therefore, a stronger signal can be captured in high atomic number materials. BSEs signal can provide composition contrast and help us distinguish different phases.

There are also characteristic X-ray and Auger electrons besides BSEs and SEs. Auger electron spectroscopy will be discussed in Section 4.2.4. When electron beam strikes on specimen surface, some atoms will release their inner shell electrons and leave a vacancy there. It is an unstable state. If the

outer shell electron migrates and fills that vacancy, X-rays could be emitted due to the higher energy of the outer shell electron. The differences in energy between specific outer shells and inner shells are characteristic. Hence, the emitted X-rays are also characteristic. The chemical composition of specimen can be obtained by considering the energy and counts of these X-rays. This is the principle of energy dispersive X-ray spectroscopy (EDX) techniques equipped on SEM instrument. The special resolution of EDX depends on the sample material and beam energy but is usually in the order of ~1 μm.

4.2.4 Auger electron spectroscopy

As depicted before, when a specimen is probed by an electron beam, inner shell electrons could be ejected and the outer shell electron, which is at high energy level, migrates to inner shell. Due to conservation of energy, the excess energy will be released by either characteristic X-ray or exciting another outer shell electron to escape from the atom. This "escaped" electron is termed the Auger electron, as shown in Figure 13. Moreover, the kinetic energy of Auger electron can be roughly calculated by the energy of core hole (E_k) and the energy level of two outer electrons (E_{L1} and E_{L2}), as expressed by Equation (10):

$$E_{KL_1L_2} \approx E_K - E_{L_2} - E_{L_1} \tag{10}$$

where $E_{KL_1L_2}$ is the kinetic energy of a KL_1L_2 Auger electron, E_{L_2} and E_{L_1} are the binding energies of two outer electrons respectively. The terms of $E_K - E_{L_2}$ is the difference in energy of migrated electron before and after transition. It is worth to notice that the calculation does not consider the interaction energy between left holes on L_1 and L_2 level in final state nor the atomic relaxation energy and extra-atomic relaxation energy. However, it expresses the mechanism of auger electron emission.

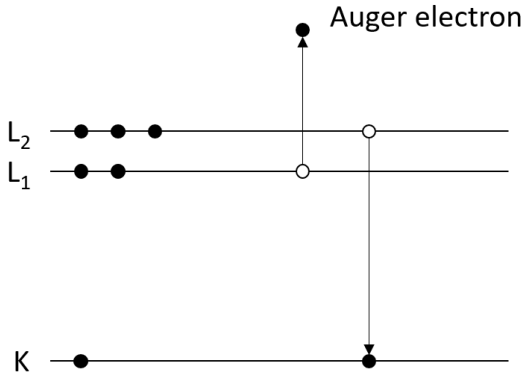

Figure 13. Schematic of Auger electron.

From Equation (10), it is known that the kinetic energy of Auger electron is not related to the energy of primary electron beam. These characteristic kinetic energies can be used to identify elements at surface. The intensity at specific kinetic energy can be used for semi-quantification of composition. Due to the low energy of Auger electrons, the escape depth is in a range of 0.5 – 8 nm. Hence, Auger electron spectroscopy (AES) is a surface sensitive technique and offers a capacity to analysis surface chemical composition with high lateral resolution. This is different from EDX. In the present study, a PHI700 instrument from Physical Electronics with lateral resolution of ~ 10 nm was used.

4.2.5 Transmission electron microscopy

As discussed in the section of SEM, various signals can be obtained when an electron beam radiates on a specimen. If the specimen is thin enough (typically less than 100 nm), the transmitted electron can penetrate through the specimen. This is the fundamental principle of TEM. The primary electrons

generated from an electron gun, which could be equipped with a tungsten filament or single crystal LaB_6 filament. These electrons are subsequently accelerated to a high energy (typically 80 – 300 KeV) and then focused into a small probe by a set of magnetic lenses. The focused beam can be transmitted through the sample and forms images in a fluorescent screen. With a higher energy, the wavelength of electrons is shorter. Hence, the images formed by these transmitted electrons have the capacity of showing fine details and even an arrangement of atoms. Apart from the conventional imaging function, TEM also has the modes of selected area electron diffraction (SAED), dark field imaging, energy-dispersive X-ray spectroscopy and so on. SAED pattern can provide the lattice structure information of specified area and the dark field imaging can show the regions that contribute to specific spot in SAED pattern. Transmission electron microscopy (TEM) is the powerful technique for microstructure analysis, phase identification and compositional investigation, especially for nanoscale features. The TEM instrument used in present study is a FEI Tecnai T20 LaB6 microscope operated at 200 KV equipped with a Orius 200 CCD camera.

4.2.6 Simulation software

Simulation by means of ThermoCalc and JMatPro can efficiently predict the microstructure and properties of target materials. Software ThermoCalc 2019a was used in this study with the access to TCFE10 database. Based on the composition and temperature, many properties can be calculated such as thermophysical properties (e.g. density, coefficient of thermal expansion, viscosity), kinetic properties (e.g. diffusion coefficients, atomic mobility), characteristics related to equilibrium and non-equilibrium solidification (e.g. freezing range, shrinkage) using different databases and theoretical models. In this study, solidification, specifically, solid fraction curves of steels were calculated under both equilibrium and non-equilibrium conditions by Scheil solidification simulation. Another simulation software, JMatPro v.11, was used to predict CCT & TTT diagrams and to simulate the precipitation behavior during the steel tempering.

4.3 Mechanical testing

Tensile testing. After the designed heat treatment (as shown in Section 4.1.5), the specimens of M-H13 steel produced by LB-PBF were post machining to prepare cylindrical tensile bars with thread-end and a gauge length of 25 mm and diameter of 5 mm. Testing was performed on an Instron 4505-5500R tensile tester with strain rates of 10^{-4} s^{-1} and 10^{-1} s^{-1} respectively in order to investigate tensile behavior including strain rate sensitivity of AM parts under different conditions. The obtained engineering stress-strain data were converted into true stress-strain data by Equation (11) and (12):

$$\sigma_t = \sigma(1 + \varepsilon) \tag{11}$$

$$\varepsilon_t = \ln(1 + \varepsilon) \tag{12}$$

where σ and ε is the engineering stress and strain while $\sigma_t$and ε_t are true stress and strain, respectively. These two equations are not valid after necking.

Impact toughness testing. The energy absorbed by the specimen before fracture can be used to evaluate the toughness of this materials. Charpy V impact toughness test is a popular method to measure the toughness in materials science and metallurgy due to its simple preparation and quick obtained result. During the test, a pendulum at a fixed known height drop down and strike on the specimen at lowest position. By measuring the angle of the pendulum at the rest travel, the energy absorbed by the broken specimen can be calculated. In present study, the specimens have a dimension of 55×10×10 mm^3. The notch located at the longitudinal side have a 2 mm depth, a 45° angle and a tip radius of 0.25 mm. The

tests were carried out on a Roell Amsler RKP instrument. The energy of the pendulum was preset to 150 J.

Hardness testing. Hardness is the ability of materials to resist local plastic deformation, which is a critical mechanical property for tool steels. In this study, Vickers hardness (HV) test was performed on a DuraScan 70-G5 machine with the ASTM E384-17 standard. During the test, a pyramidal diamond indenter was pressed into specimen with a chosen load F, which is 10 kg in this thesis, to form a square indentation. Then the hardness (HV in kgf/mm^2) was calculated by Equation (13) using the average diagonal length *d* measured from the indentation.

$$HV \approx \frac{1{,}8544F}{d^2} \tag{13}$$

Every hardness value is the average of more than 6 measurement [80].

Chapter 5 - Results

This chapter includes the results of two appended papers which deal with tool steels fabricated by AM. In **Paper I**, parts of M-H13 hot work tool steel were produced by LB-PBF. The effect of two type of post processing, direct tempering from as-built condition (DT) and conventional quenching followed by tempering (QT), on the microstructure and mechanical properties was evaluated. In addition, the softening behavior of the steel with two post treatment routes at elevated temperatures of 550 ℃ and 600 ℃ was assessed. In **Paper II**, V4E cold work tool steel was cladded on Dievar steel substrate by means of DED. The defects (e.g., porosity and cracking) in the deposited zone were characterized and the formation of these defects was discussed.

5.1 The microstructure of the as built parts

In **Paper I** and **Paper II**, the microstructures of the as-built M-H13 hot work tool steel and V4E cold work tool steel parts were studied. The investigation demonstrates M-H13 steel parts fabricated by LB-PBF has a cellular structure with a cell size of ~0.7 µm (Figure 14 a & b). Meanwhile, a considerable proportion of retained austenite was found, which means the intrinsic austenitizing and tempering during the LB-PBF process could not eliminate the retained austenite due to insufficient time. This explains the relative low hardness (500 HV_{10}) of as-built M-H13 steel. In **Paper II**, the V4E steel produced by DED shows near columnar dendrite structure with a secondary arm space of ~ 4 µm (Figure 15). This structure will be further discussed in section 5.2.(Figure 20). Retained austenite mixed with carbides was also found at the interdendritic regions.

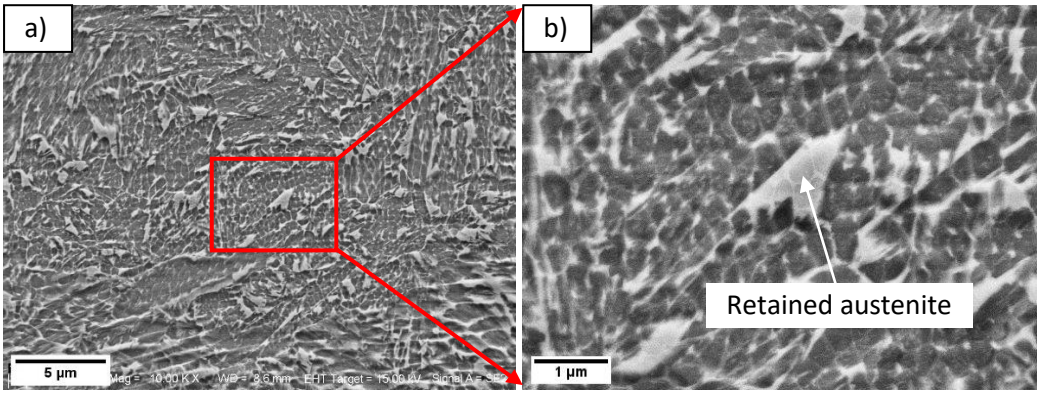

Figure 14. (a)&(b) SEM images of as-built M-H13 steel produced by LB-PBF under the VED of 67 J/mm^3.

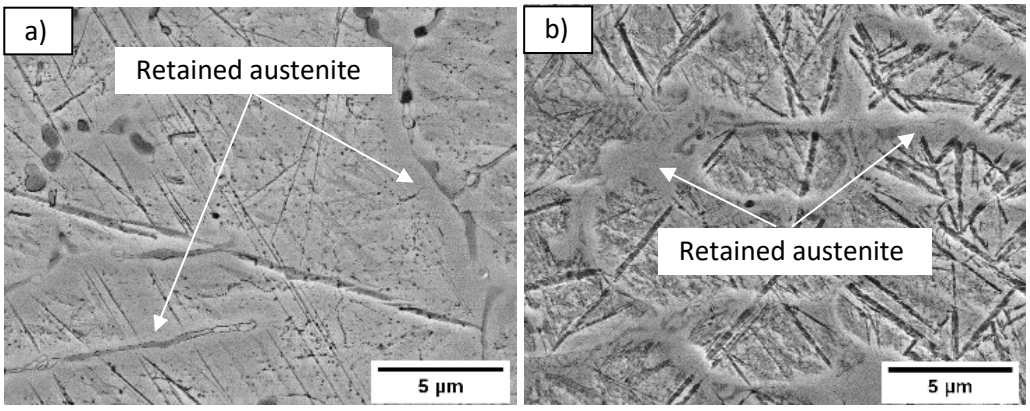

Figure 15. SEM images from the top layer of as-built V4E steel produced by DED. (a) the microstructure of the region less effected by the next melt track. (b) the heat affected region by the next track.

Volumetric energy densities (VED) can be calculated. In the current study, this value was similar for V4E steel manufactured by DED (57 J/mm^3) and M-H13 produced by LB-PBF method (67 J/mm^3). The different morphology of as-built microstructure is supposed to attributed to different cooling rates in LB-PBF and DED method. The dimension of melt pool in DED is much larger than that of LB-PBF, leading to a lower heat transfer efficiency to surrounding solid and consequently a lower cooling rate. Therefore, the morphology of dendrites changed from cellular in M-H13 steel to columnar dendrite in V4E steel. Furthermore, the size of dendrite structure can also reflect the cooling rate. If the cellular structure were assumed as the primary arm of columnar dendrite, the space (~0.7 μm) in M-H13 steel is even smaller than the secondary arm space of columnar dendrite (~ 4 μm) in V4E (Figure 14 and 15).

5.2 Defects in as-built samples

Defects, including cracks, pores and lack of fusion etc, are commonly observed in as-built part. Figure 16 shows some pores located preferentially in large melt pools in M-H13 steel produced by LB-PBF. These pores are considered as keyhole pores. Relative density (measured by ImageJ software) of as-built M-H13 parts is as high as 99.94 %.

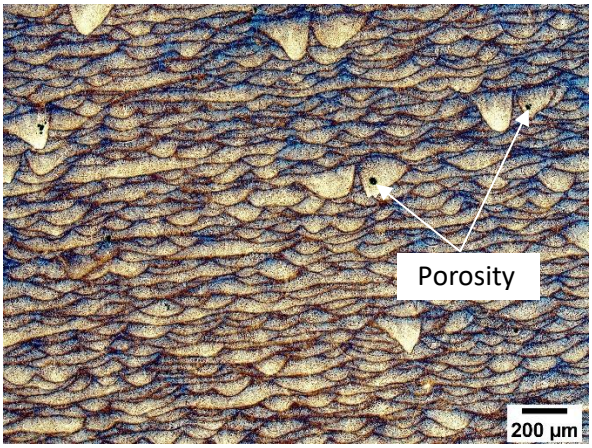

Figure 16. Cross section of as-built M-H13 parts fabricated by LB-PBF.

Figure 17 shows both cracks and voids observed in V4E cladded zone fabricated by DED method. With the increase of layers, more defects are found. For 1-layer sample (Figure 17a), a near fully density without distinct defect was seen. For 2-layers sample, some defects including voids and some tiny cracks occur in the deposited zone (DZ), especially at the 2nd layer (Figure 17b). When the number of cladding layers increases to 4, the amount of defects increases significantly. However, the large voids are preferentially located at the bottom region of the layers (Figure 17c). In this sample, the number of cracks also increases. The cracks are roughly parallel to the building direction. Based on the analysis using ImageJ, the relative densities of the samples are 99.44 %, 99.65 % and 98.73 % for 1-, 2- and 4 layers, respectively. From the perspective of relative density, it is recommended that no more than 2 layers of V4E steel (in a total thickness of ~ 3 mm can be cladded on top of Dievar). It could be pointed out that when more than one layer is being deposited, the deposition of the layers after the first layer takes place on the "cold work" deposit layer which is expected to be more brittle compared to the hot work base material. This condition can be compared to DED on a cold work tool steel which is challenging due to the generally low weldability of this family of tool steel.

There are mainly three type of pores in 4-layers samples, large irregular pores, round keyhole pores and shrinkage pores. These defects would cause stress concentration when suffering internal or external stress, being the initiation places for failures. On the surface of one irregular large pore (larger than 50

μm) prepared by breaking the sample with a hammer, SEM imaging and EDX mapping indicated the relative smooth pore surface contained higher amount of Si and O, as shown in Fig. 18. This suggested the existence of oxide. In addition, higher Mo and V concentration was also found in point A by EDX point analysis. To identify the oxide formed at the internal surface of this pore, AES depth-profiling was performed, and the result is presented in Fig. 19. At the top surface of this area, only Si and O were found, indicating the formation of Si oxide film. With the increase of depth, the concentration of Si and O are declined synchronously. The thickness of Si oxide is about 20 nm, below which a layer enriched in C, Fe and V was found. The thickness of this layer is about 140 nm. Matrix dominant in Fe was reached at the depth of ~ 160 nm.

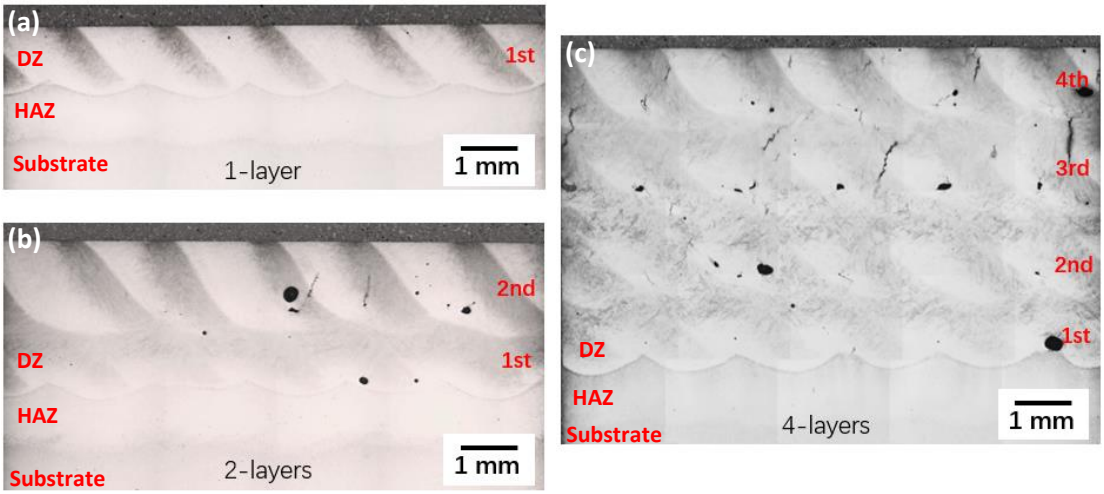

Figure 17. Cross-sections of cladded V4E steel fabricated with: (a) 1-layer, (b) 2-layers, (c) 4-layers. DZ: deposited zone, HAZ: heat affected zone.

However, it seemed that not all pores had this silicon oxide film. Oxygen could not be detected by EDX at shrinkage pores and spherical pores with small size. For the irregular large pores, the Si element in V4E steel was oxidized selectively and gathered at the internal surface of void during melting. This oxide film could change the interfacial energy of melt pool and consequently the flow behavior of the melt, preventing the elimination of the pores [81]. It is seen from Figure 17 that most of these large

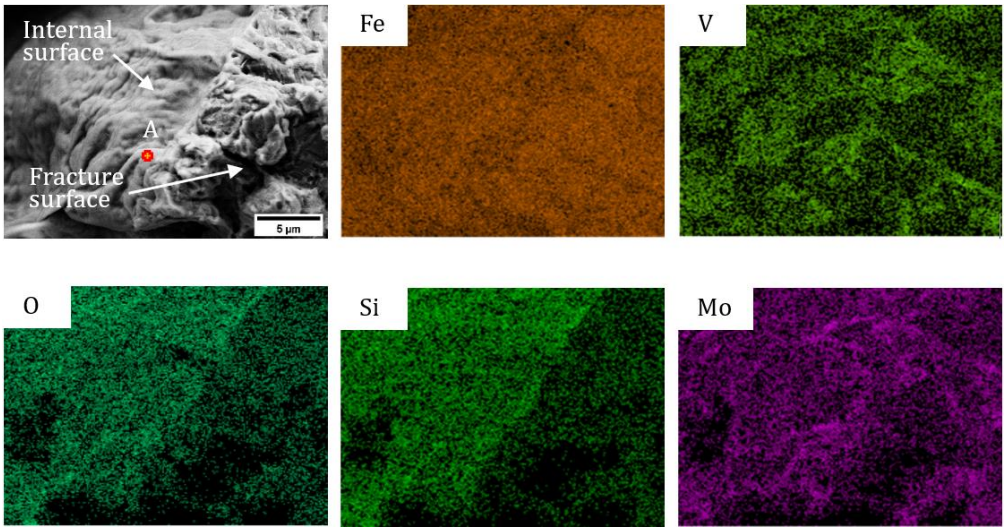

Figure 18. SEM image and associated EDS maps of the main alloying elements of a region located at the void boundary. Point A is from the surface of a large irregular pore.

pores are located at the bottom of each layer. In general, the voids in melt pool is supposed to float on the newly deposited layer. If the heat input is insufficient, or the void is adjacent to melt pool boundary, there is no sufficient time for the voids to float up to melt pool surface and it will be trapped at the bottom of melt pool. For shrinkage pores, it is generally believed that the formation is caused by the insufficient liquid refill during the solidification.

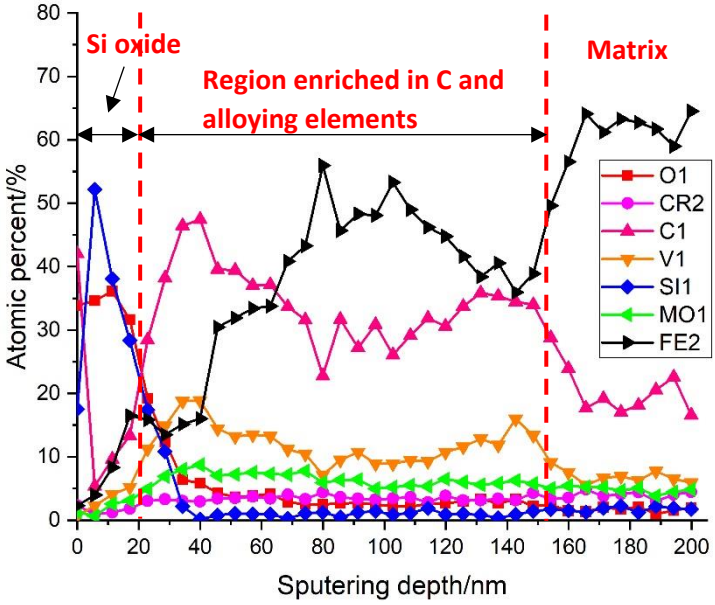

Figure 19. AES depth-profile from the internal surface of the void at point A in Figure 18.

Cracking was another big issue in DED V4E, the tendency of which increased with building height (Figure 17). It occurred during solidification and was related to the microstructural change and the intrinsic characteristics of V4E (wide temperature range of solidification). Figure 20 exhibited the microstructure of deposited V4E with different layers. The 1st layer (Figure 20a) adjacent to substrate has a cellular structure with carbides in the shape of short rods along cell boundaries. For the second and third layer, the cellular structure is coarser, and the carbides become longer. In the top layer, columnar dendrite was formed. Heat transfer plays a critical role for microstructure evolution. The fine cellular structure in the 1st layer (bottom layer) is due to its high cooling rate, which is attributed to low temperature of substrate. For the subsequent layers, the cooling rate and temperature gradient decrease correspondingly because the new layers are deposited on the previous hot layers. This leads to the coarsening of the cellular structure and even for the generation of columnar dendrite, as shown in Figure 20. It is expected that this change in structure alters the hot crack susceptibility. There is a short backfill channel in fine cellular structure when the solidification is in the last stage (solid fraction > 0.8). Liquid can then easily be supplied into the cavity caused by the volumetric solidification shrinkage and thermal contraction. In contrast, the columnar dendrite has a long channel for supplement, which can be easily closed by the growth of columnar dendrite. The trapped liquid in the interdendritic region then forms a cavity, which could lead to cracking. In the present study, compared to fine cellular structure, coarser structure and columnar dendrite structure exhibited higher cracking susceptibility. This is one important reason for cracking in upper deposited layers during solidification. Another reason is the intrinsic properties of materials. It is well known that metallic materials with a large range of solidification temperature will have a high cracking susceptibility, because the liquid film at the last solidification stage (solid fraction > 95 %) will be preserved to low temperature during the solidification process. This is accompanied by increased thermal stress, leading to cracking at the site of vulnerable liquid film.

The solidification temperature range of V4E steel was simulated by Scheil simulation from ThermoCalc. It has been found that the temperature range of Scheil solidification (234 ℃) is significantly larger than that of equilibrium condition (142 ℃). More details are presented in **Paper II**.

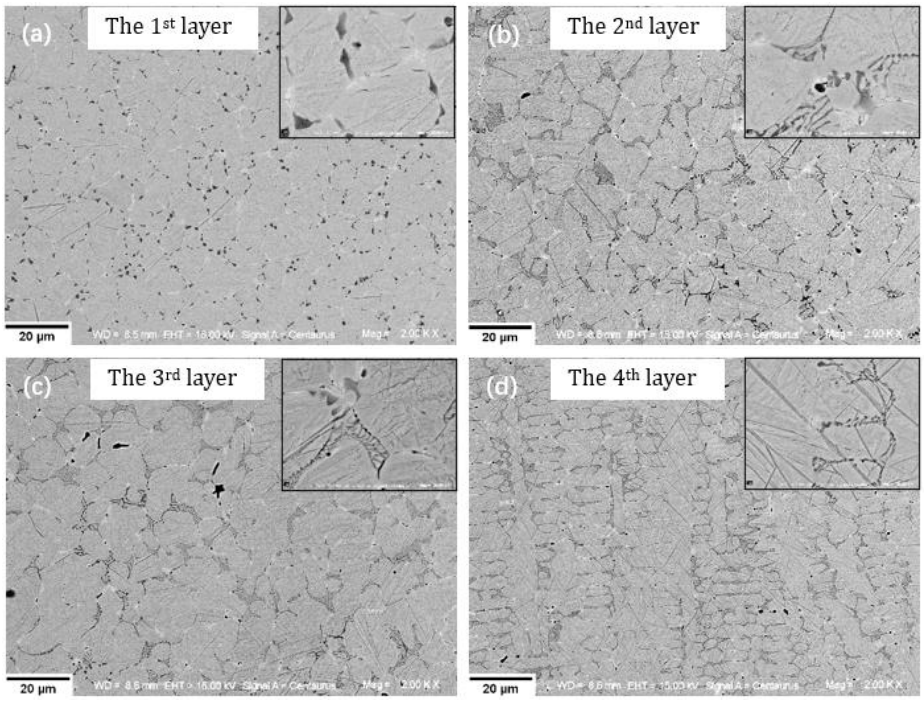

Figure 20. Comparison of the microstructure from different deposited layers: (a) the 1st layer, (b) the 2nd layer, (c) the 3rd layer, (d) the 4th layer.

5.3 Effect of post heat treatments on the microstructure and mechanical properties of M-H13 steel fabricated by LB-PBF

Two post-AM heat treatments (DT and QT) were conducted on as-built M-H13 steel to investigate the effect on the microstructure and mechanical properties. The purpose of DT heat treatment is to eliminate retained austenite and release internal stress. It is also for simplification of the process. Regarding QT heat treatment, it is the common hardening heat treatment route conducted on conventional tool steels. Essentially, the parts after QT heat treatment are supposed to be equivalent to traditional ones because

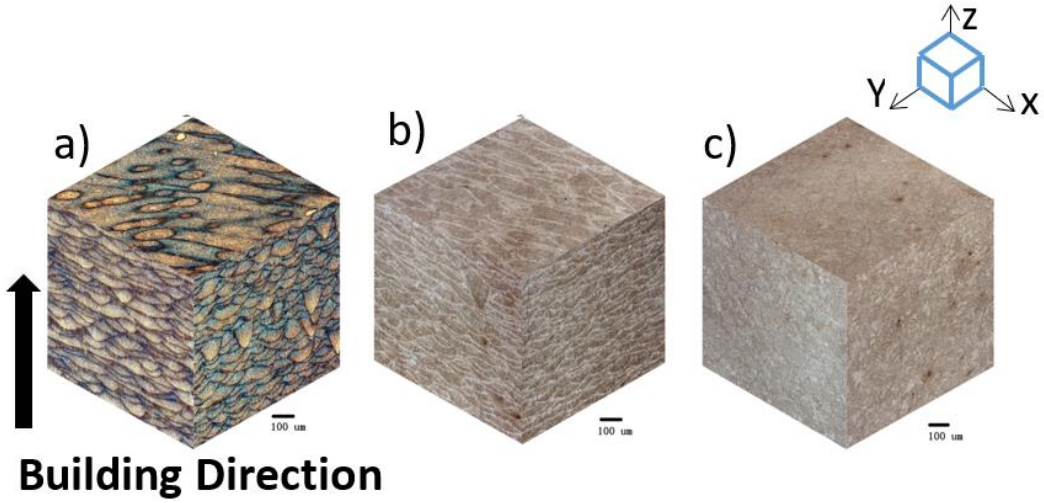

Figure 21. The optical microscopic images of (a) as built, (b) DT, (c) QT state in the XZ, YZ and XY planes.

the structure obtained from LB-PBF process should be removed by high temperature austenitizing. Therefore, the comparison of the properties and structure of DT and QT sample in fact provides the difference between the LB-PBF sample and the traditional one. As we can see in Figure 21, after DT heat treatment, the melting-pool morphology was well preserved. However, the QT sample shows a homogeneous structure and the melting-pool morphology was completely removed.

SEM was employed to investigate the microstructure of M-H13 steel in detail at different state, as shown in Figure 22. After DT heat treatment, retained austenite was removed, and the fine cellular structure was clearly revealed in Figure 22b. For the QT sample, the previous cellular structure from as-built state was completely removed and replaced by a full martensite structure presented in Figure 22d. Moreover, some carbides in rod shape were precipitated along the martensite boundaries forming a lath structure.

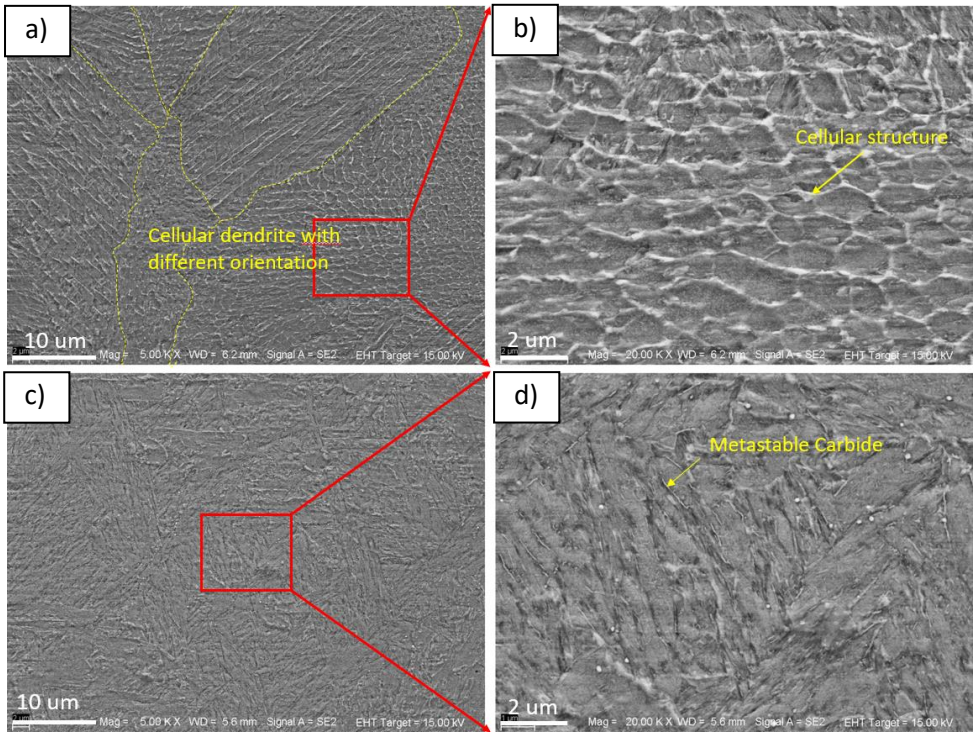

Figure 22. SEM images showing the microstructure of LB-PBF M-H13 tool steel under different heat treatment: (a) DT, (c) QT, (b)&(f) the corresponding high magnification view.

In **Paper I**, the mechanical properties (e.g., tensile strength, impact toughness and hardness) have been tested. Figure 23 shows the true stress-strain curves under the uniaxial tensile load with two different strain rates of 10^{-4} s^{-1} and 10^{-1} s^{-1}. Under quasi-static tension (10^{-4} s^{-1}), the (engineering) yield strength and tensile strength of DT sample is 1529 MPa and 1732 MPa, respectively. For the QT sample, the corresponding data is 1449 MPa and 1681 MPa, which are slight lower than the DT sample. From the reference [6], the yield and tensile strength of wrought H13 in hardened condition are in the range of 1290-1570 MPa and 1500-1960 MPa, respectively. In addition, both DT and QT sample have a elongation of 10-11 %, which is similar as that for wrought H13 steel (13%). Hence, the LB-PBF M-H13 steel in both DT and QT condition have a comparable tensile property to the wrought counterpart in hardened condition. However, the hardening mechanisms under these two post heat treatments are different. The high strength in DT sample is attributed to tempered martensite and the fine cellular structure. A vast boundary of cellular structure can be the barrier for dislocation movement. Regarding the QT sample, martensite structure and the precipitates along the martensite boundary are key sources

for high strength. How long these two strengthening mechanisms can be maintained at high temperatures is supposed to be the key factor for softening resistance, which will be discussed in section 5.4. When the strain rate was changed to 10^{-1} s^{-1}, the yield strength and tensile strength of both DT and QT sample have an increase. Strain rate sensitivity calculated is 0.00498 for DT and 0.00767 for QT sample, respectively. This means stronger strain rate hardening effect in QT sample. In addition, it also has higher work hardening ability. Fitting tensile curves using Hollomon's equation ($\sigma = K\varepsilon^n$) gives the strain hardening exponent n under different conditions, as shown in Table 4. The n value of QT sample is higher than that of DT at both strain rates. Higher strain rate sensitivity and higher strain hardening ability of QT sample give a reasonable explanation to the improved impact toughness of QT sample in Charpy impact test, which has a much higher strain rate of 10^2 - 10^4 s^{-1}.

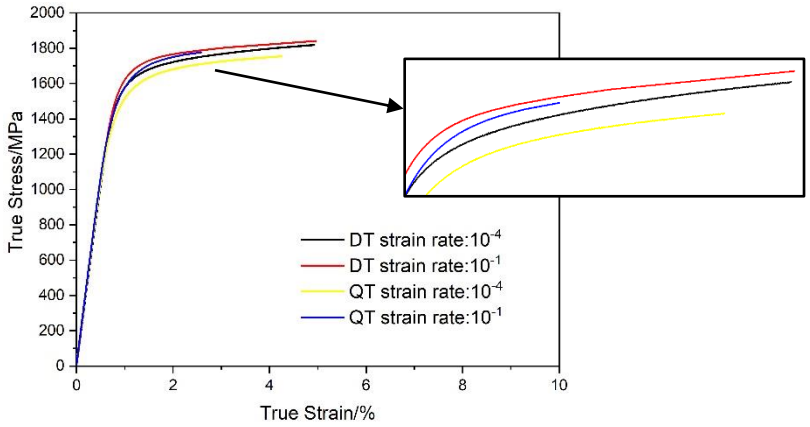

Figure 23. The true stress-strain curves of M-H13 steel suffered different post heat treatment routes in the strain rate of 10^{-4} s^{-1} and 10^{-1} s^{-1}.

Table 4. The mechanical properties of M-H13 steels under variable conditions.

Sample	Strain rate /s^{-1}	$R_{p0.2}$ /MPa	R_m /MPa	δ/%	True $R_{p0.2}$/MPa	True R_m/MPa	Strain hardening exponent	Strain rate sensitivity
DT	10^{-4}	1529	1732	10.2	1532	1820	0.094	0.00475
DT	10^{-1}	1580	1752	10.4	1583	1841	0.081	
QT	10^{-4}	1449	1681	11.2	1452	1755	0.111	0.00767
QT	10^{-1}	1526	1731	10.8	1529	1776	0.111	

5.4 Softening of M-H13 steel fabricated by LB-PBF at elevated temperatures

Hot work tools are exposed to work material heat treated at high temperatures. An excellent thermal softening resistance is therefore a critical property for M-H13 steel in such application. In **Paper I**, the softening resistance was evaluated by the hardness during a long-term exposure at 550 ℃ and 600 ℃, respectively. Figure 24 shows the hardness evolution of LB-PBF M-H13 steel at various conditions. It is dependent on the post-AM treatment and the conditions of subsequent exposure at high temperatures. Longer time or higher temperature exposure make the hardness decrease more. Less softening was observed for 550 ℃ hold than that for 600 ℃ hold. The decrease of hardness is more severe for QT samples. DT sample at 550 ℃ has the best softening resistance and the hardness drop after 100 h is only about 47 HV_{10}, while the corresponding value for QT sample is 74 HV_{10}, which is 64.7% higher

than DT sample. The same tendency is also found at 600 ℃. There is a dramatical decrease of hardness for the both DT and QT sample at this temperature, especially in the first 25 h.

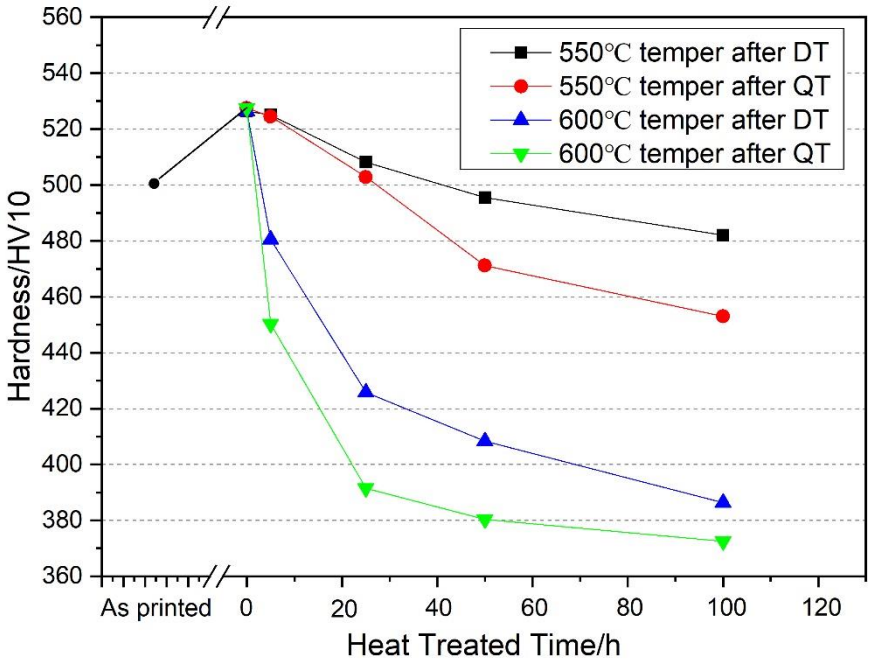

Figure 24. The hardness evolution of LB-PBF M-H13 steel at various conditions. As-built sample has a hardness of 502 HV_{10} due the existence of retained austenite. After DT and QT treatment, the steel has the highest hardness about 527 HV_{10}.

It is supposed that smaller grain size of ferrite, the cellular structure being preserved, and possibly less coarsened carbides make DT samples more thermal softening resistant. The martensite formed during printing decomposed into ferrite and carbides in both DT and QT sample. Absence of austenitizing makes the final ferrite grain size smaller than that form QT. This can be illustrated by the half maxima (FWHM) of bcc diffraction lines from XRD pattern. At both 550 ℃ and 600 ℃, DT sample has smaller

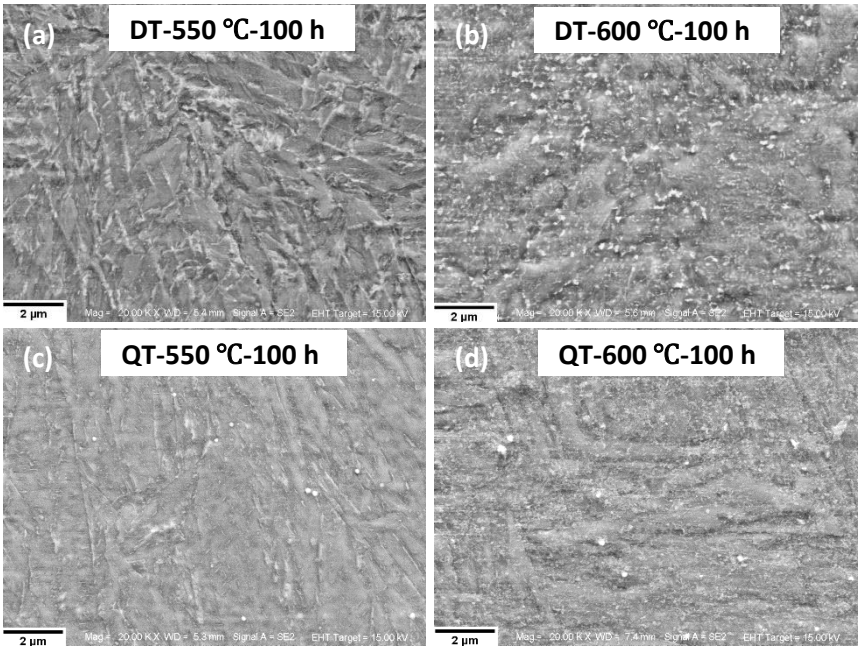

Figure 25. SEM images of DT and QT sample after 100 h heat treatment at 550 ℃ and 600 ℃.

FWHM compared to QT. This means the DT samples have a finer grain size, leading to higher hardness and consequently a better thermal softening resistance than QT sample. Moreover, the softening resistance of steels depends on the stability of the microstructure. As seen from Figure 25a, the fine cellular structure obtained from the solidification process due to its high cooling rate can be seen even after a heat treatment at 550 ℃ for100 h, though it partially dissolved. This structure help maintain the hardness at this temperature. For the QT sample treated at 550 ℃ for100 h, the lath structure was coarser and less easy to be observed and carbide in a shape of rod along the martensite boundary are dissolved, as shown in Figure 25c.

At the higher temperature of 600 ℃, the hardness behavior of both DT and QT sample are deteriorated rapidly. From the perspective of microstructure, cellular structure disappears from DT (Figure 25b). Ferrite becomes coarser for both DT and QT samples, as indicated by FWHM of bcc diffraction lines from XRD pattern (see **Paper I**). It is believed that the hardness change is also related to the carbides evolution which is rather complicated. By combined experimental and numerical methods, it has been found that in QT process, the carbides formed are likely to be M_7C_3 which might be too small to be observed, and M_3C carbide in a shape of rod. When subjecting to high temperature exposure, metastable M_7C_3 and M_3C carbide will dissolve into matrix. Fine $M_{23}C_6$ and M (C, N) would be formed. With the increase of temperature to 600 ℃, carbide may become coarser. In all condition, M_6C can be identified.

Chapter 6 - Conclusions

From the study in this thesis, the following conclusions can be drawn:

High density parts of M-H13 hot work tool steel can be fabricated by LB-PBF method. The as-built samples have a fine cellular structure with a considerable content of retained austenite. Subsequently, the built samples were post heat treated by direct tempering (DT) route and quenching and tempering (QT) route, respectively. The typical microstructure in QT condition was tempered martensite with carbides along lath boundaries. In DT condition, melt pool boundaries and cellular structure from as-built condition were still observed. While comparable tensile properties and hardness were obtained, DT samples exhibited significantly lower impact toughness compared to QT samples. This was attributed to the difference in work hardening ability and strain rate sensitivity originating from different microstructures obtained under these two heat treatment conditions.

Thermal softening resistance is dependent on the post-AM treatment and the conditions of subsequent exposure at high temperatures. Longer time or higher temperature exposure make the hardness decrease more. Less softening was observed for 550 ℃ hold than that for 600 ℃. The decrease of hardness is more severe for QT samples. It is supposed that smaller grain size of ferrite, less coarsened carbides and the cellular structure being preserved make DT samples more thermal softening resistant.

Defects (voids and cracks) were observed in the cladded zone of V4E steel produced by DED, especially with the increase of building height. For the large irregular pores, a thin Si oxide layer was found at the top of the internal surface, below which a layer enriched with alloy elements and C was detected. The formation of this type of pores is attributed to insufficient heat input and preventing effect of pore elimination caused by the oxide layer and alloy elements enriched layer on the pore surface. Non-equilibrium eutectic microstructure is a characteristic feature in the region adjacent to the pores. There are two important contributing factors for cracking. First, the microstructure of bottom layer to top layer changes from fine cellular to columnar dendrite. Second, the deposited cold work tool steel has a relatively large temperature range of solidification, as simulated by using ThermoCalc. The studied cold work tool steel seems to be sensitive to hot cracking.

Chapter 7 - Future Work

Since LB-PBF studies on hot work steel are increasing being reported in literature, it is suggested that further studies focus on DED solutions for hot forming applications. The aim would be to find the optimum choice of a material, process and post treatment "solution" that provides a combination of wear and softening resistance at elevated temperatures.

In the present licentiate thesis, defect formation in the deposited zone is analyzed when V4E cold work tool steel is used suggests that these defects are caused by both- the intrinsic properties of material (e.g., large solidification temperature range) and inappropriate process parameters (e.g., without preheating substrate). Hence, it is necessary to continue the investigation by varying the hardfacing materials, such as tool steel with different hard phase constituents and even maraging tool steels. Also, a suitable preheating of the base plate should be carried out to understand the influence on process ability and microstructure.

Due to their application in hot stamping, it is important to assess the softening resistance of the subsequent cladded materials by comparing their hardness behavior in long-term heat treatment at elevated temperatures. Meanwhile, investigating the evolution of microstructure of hardfacing materials produced by DED will help us to understand the strengthening mechanisms of different tool steels. Before that, finding optimized post heat treatment routes for these cladded materials is also needed.

At the last step, the wear resistance of cladded materials against the material of stamping blank sheet at elevated temperatures will be tested as well. It will assess which material is suitable for the hardfacing of Dievar in the application of hot stamping. Of course, the wear mechanisms during the test will be studied.

Acknowledgements

First, I would like to thank my supervisors Prof. Yu Cao and Libin Liu and my co-supervisor Prof. Lars Nyborg for giving me the opportunity to take part in this interesting project and their valuable guidance and help during this special time.

I would also like to thank Uddeholms AB and RISE IVF AB for providing the funding and framework under which projects have been conducted. Special thanks go to Dr. Seshendra Karamchedu for his collaboration in terms of planning, guidance and for providing the materials that were needed in this research. I would like to thank Petter Damm and Aydin Selte from Uddeholms AB, Eason Fan, Wei Lun from ASSAB Tooling Technology. and Ye WeiJiang Jason, voestalpine High Performance Metals for their feedback during monthly work meetings.

Furthermore, I would like to acknowledge the research engineers Dr. Yiming Yao, who help me do TEM experiments, Eric Tam, Håkan Millqvist and Roger Sagdahl for their support in terms of practical work in this research.

Many thanks to the colleagues at Department of Industrial and Materials Science, especially for Xiuyu, Jinhua, Kristoffer, Zhenyuan, Jaime and Hans, for their supporting and encouraging for me to make the day in Sweden more enjoyable.

Finally, I would like to thank my families for their love, support and help even from the really long distance.

References

[1]. P. Kattire, S. Paul, R. Singh, and W. Yan, “Experimental characterization of laser cladding of CPM 9V on H13 tool steel for die repair applications,” J. Manuf. Process., vol. 20, pp. 492–499, 2015.

[2]. J. J. Yan et al., “Selective laser melting of H13: microstructure and residual stress,” J. Mater. Sci., vol. 52, no. 20, pp. 12476–12485, 2017.

[3]. T. Roy et al., “Effect of deposition material and heat treatment on wear and rolling contact fatigue of laser cladded rails,” Wear, vol. 412–413, no. May, pp. 69–81, 2018.

[4]. M. Åsberg, G. Fredriksson, S. Hatami, W. Fredriksson, and P. Krakhmalev, “Influence of post treatment on microstructure, porosity and mechanical properties of additive manufactured H13 tool steel,” Mater. Sci. Eng. A, vol. 742, no. August 2018, pp. 584–589, 2019.

[5]. K. Kempen, B. Vrancken, S. Buls, L. Thijs, J. Van Humbeeck, and J. P. Kruth, “Selective Laser Melting of Crack-Free High Density M2 High Speed Steel Parts by Baseplate Preheating,” J. Manuf. Sci. E-T ASME, vol. 136, no. 6, pp. 061026, 2014.R. Mertens, B. Vrancken, N. Holmstock, Y. Kinds, J. P. Kruth, and J. Van Humbeeck, “Influence of powder bed preheating on microstructure and mechanical properties of H13 tool steel SLM parts,” Phys. Procedia, vol. 83, pp. 882–890, 2016.

[6]. L. Xue, “Laser consolidation: A rapid manufacturing process for making net-shape functional components,” Adv. Laser Mater. Process. Woodhead Publishing, pp. 492–534, 2010.

[7]. J. Lee et al., “Microstructural effects on the tensile and fracture behavior of selective laser melted H13 tool steel under varying conditions,” Materials Characterization, vol. 155, pp. 109817, 2019.

[8]. S. Kou, “Welding metallurgy”. New Jersey, USA, pp.431-446, 2003.

[9]. S. Giganto, P. Zapico, M. Á. Castro-Sastre, S. Martínez-Pellitero, P. Leo, and P. Perulli, “Influence of the scanning strategy parameters upon the quality of the SLM parts,” Procedia Manuf., vol. 41, pp. 698–705, 2019.

[10]. W. Do Yoo, J. H. Lee, K. T. Youn, and Y. M. Rhyim, “Study on the microstructure and mechanical properties of 17-4 PH stainless steel depending on heat treatment and aging time,” Solid State Phenom., vol. 118, pp. 15–20, 2006.

[11]. H. Chen, D. Gu, D. Dai, C. Ma, and M. Xia, “Microstructure and composition homogeneity, tensile property, and underlying thermal physical mechanism of selective laser melting tool steel parts,” Mater. Sci. Eng. A, vol. 682, no. November 2016, pp. 279–289, 2017.

[12]. C. Barr, S. Da Sun, M. Easton, N. Orchowski, N. Matthews, and M. Brandt, “Influence of macrosegregation on solidification cracking in laser clad ultra-high strength steels,” Surf. Coatings Technol., vol. 340, no. July 2017, pp. 126–136, 2018.

[13]. Z. Liu and H. Qi, “Effects of substrate crystallographic orientations on crystal growth and microstructure formation in laser powder deposition of nickel-based superalloy,” Acta Mater., vol. 87, pp. 248–258, 2015.

[14]. R. Mertens, B. Vrancken, N. Holmstock, Y. Kinds, J. P. Kruth, and J. Van Humbeeck, “Influence of powder bed preheating on microstructure and mechanical properties of H13 tool steel SLM parts,” Phys. Procedia, vol. 83, pp. 882–890, 2016.

[15]. British standard BS EN ISO 4957:2000, Tool Steels; British Standards Institution, European Standard EN ISO 4957:1999E (English version). Tool Steels; European Committee for Standardization: Brussels.

[16]. L.S. Figiel, “On Damascus Steel,” Atlantis Arts Press, 1991.

[17]. J.M. Yumoto, “The Samurai Sword,” Charles E. Tuttle Company: Tokyo, Japan, 1958.

[18]. A. S. Townsend, “Alloy Tool Steels and the Development of High-Speed Steel,” Trans. Am. Soc. Steel Treat, Vol. 21, pp. 769-795, 1933.

[19]. Uddeholm, “Vanadis 4 Extra SuperClean,” pp. 1–8, 2016.

[20]. J. O. Milewski, “Additive manufacturing of metals,” Appl. Mech. Mater., 2017.

[21]. M. Jamshidinia, A. Sadek, W. Wang, S. Kelly. “Additive manufacturing of steel alloys using laser powder-bed fusion,” Adv. Mater. Process, vol. 173(1), pp. 20–24, 2015.

[22]. C. Kamath, B. El-dasher, G.F. Gallegos, W.E. King, A. Sisto, “Density of additively-manufactured, 316L SS parts using laser powder-bed fusion at powers up to 400 W,” Int. J. Adv. Manuf. Technol., vol. 74, pp. 65–78, 2014.

[23]. S. A. Khairallah, A. T. Anderson, A. M. Rubenchik, and W. E. King, “Laser powder-bed fusion additive manufacturing: Physics of complex melt flow and formation mechanisms of pores, spatter, and denudation zones,” Acta Mater., pp. 613–628, 2017.

[24]. T.M. Mower, M.J. Long, “Mechanical behavior of additive manufactured, powder-bed laser-fused materials”. Mater. Sci. Eng. A, vol. 651, pp.198–213, 2016.

[25]. S. E. Brika, M. Letenneur, C. A. Dion, and V. Brailovski, “Influence of particle morphology and size distribution on the powder flowability and laser powder bed fusion manufacturability of Ti-6Al-4V alloy,” Addit. Manuf., vol. 31, no. August 2019, pp. 100929, 2020.

[26]. K. Riener et al., “Influence of particle size distribution and morphology on the properties of the powder feedstock as well as of AlSi10Mg parts produced by laser powder bed fusion (LB-PBF),” Addit. Manuf., vol. 34, no. April, pp. 101286, 2020.

[27]. X. Zhao, J. Chen, X. Lin, and W. Huang, “Study on microstructure and mechanical properties of laser rapid forming Inconel 718,” Mater. Sci. Eng. A, vol. 478, no. 1–2, pp. 119–124, 2008.

[28]. A. B. Spierings, N. Herres, and G. Levy, “Influence of the particle size distribution on surface quality and mechanical properties in AM steel parts,” Rapid Prototyp. J., vol. 17, no. 3, pp. 195–202, 2011.

[29]. K. Abd-Elghany and D. L. Bourell, “Property evaluation of 304L stainless steel fabricated by selective laser melting,” Rapid Prototyp. J., vol. 18, no. 5, pp. 420–428, 2012.

[30]. A. J. Pinkerton and L. Li, “Direct additive laser manufacturing using gas- and water-atomised H13 tool steel powders,” Int. J. Adv. Manuf. Technol., vol. 25, no. 5–6, pp. 471–479, 2005.

[31]. M. Lutter-Günther, M. Horn, C. Seidel, et al. “Influence of particle size distribution on powder flowability and part properties in laser beam melting,” Rapid. Tech. —international trade show and conference for additive manufacturing, pp. 297-311, 2017.

[32]. E. Bojestig, Y. Cao, and L. Nyborg, “Surface chemical analysis of copper powder used in additive manufacturing,” Surf. Interface Anal., vol. 52, no. 12, pp. 1104–1110, 2020.

[33]. Y. Cao, M. Delin, F. Kullenberg, and L. Nyborg, “Surface modification of Ti-6Al-4V powder during recycling in EBM process,” Surf. Interface Anal., vol. 52, no. 12, pp. 1066–1070, 2020.

[34]. X. He, J. T. Norris, P. W. Fuerschbach, T. DebRoy, “Liquid metal expulsion during laser spot welding of 304 stainless steel,” J. Phys. D. Appl. Phys., vol. 39, no. 3, pp. 525–534, 2006.

[35]. K. A. Mumtaz, N. Hopkinson, “Selective laser melting of thin wall parts using pulse shaping,” J. Mater. Process Technol., vol. 210, no. 3, pp. 279-287, 2010.

[36]. T. Debroy et al., “Progress in Materials Science Additive manufacturing of metallic components – Process , structure and properties,” Prog. Mater. Sci., vol. 92, pp. 112–224, 2018.

[37]. V. Manvatkar, A. De, and T. Debroy, “Heat transfer and material flow during laser assisted multi-layer additive manufacturing,” J. Appl. Phys., vol. 116, no. 12, 2014.

[38]. K. Ettaieb, S. Lavernhe, C. Tournier, U. Paris-saclay, E. N. S. Paris-saclay, and I. Farman, “A fl ash-based thermal simulation of scanning paths in LPBF additive manufacturing,” no. February, 2021.

[39]. M. Letenneur, A. Kreitcberg, and V. Brailovski, “Optimization of laser powder bed fusion processing using a combination of melt pool modeling and design of experiment approaches: Density control,” J. Manuf. Mater. Process., vol. 3, no. 1, 2019.

[40]. I. Yadroitsev, I. Yadroitsava, P. Bertrand, and I. Smurov, “Factor analysis of selective laser melting process parameters and geometrical characteristics of synthesized single tracks,” Rapid Prototyp. J., vol. 18, no. 3, pp. 201–208, 2012.

[41]. N. T. Aboulkhair, N. M. Everitt, I. Ashcroft, and C. Tuck, “Reducing porosity in AlSi10Mg parts processed by selective laser melting,” Addit. Manuf., vol. 1, pp. 77–86, 2014.

[42]. O. Hildreth, A. Nassar, K. Chasse, and T. Simpson, “Dissolvable metal supports for 3D direct metal printing,” 3d Print Addit. Manuf., vol. 3, nr. 2, pp. 90-97, 2016.

[43]. A. Mertens, S. Reginster, Q. Contrepois, T. Dormal, O. Lemaire, and J. Lecomte-Beckers, “Microstructures and mechanical properties of stainless steel AISI 316L processed by selective laser melting,” Mater. Sci. Forum, vol. 783–786, pp. 898–903, 2014.

[44]. M. Mazur, P. Brincat, M. Leary, M. Brandt, “Numerical and experimental evaluation of a conformally cooled H13 steel injection mould manufactured with selective laser melting,” Int. J. Adv. Manuf. Technol., vol. 93, pp. 881–900, 2017.

[45]. R. Mertens, B. Vrancken, N. Holmstock, Y. Kinds, J. P. Kruth, and J. Van Humbeeck, “Influence of powder bed preheating on microstructure and mechanical properties of H13 tool steel SLM parts,” Phys. Procedia, vol. 83, pp. 882–890, 2016.

[46]. J. Šafka, M. Ackermann, L. Voleský, “Structural properties of H13 tool steel parts produced with use of selective laser melting technology,” J. Phys. Conf. Ser., vol. 709, 2016.

[47]. M. J. Holzweissig, A. Taube, F. Brenne, M. Schaper, and T. Niendorf, “Microstructural Characterization and Mechanical Performance of Hot Work Tool Steel Processed by Selective Laser Melting,” Metall. Mater. Trans. B Process Metall. Mater. Process. Sci., vol. 46, no. 2, pp. 545–549, 2015.

[48]. R. Dörfert, J. Zhang, B. Clausen, H. Freiße, J. Schumacher, and F. Vollertsen, “Comparison of the fatigue strength between additively and conventionally fabricated tool steel 1.2344,” Addit. Manuf., vol. 27. pp. 217–223, 2019.

[49]. L. Xue, J. Chen, and S. H. Wang, “Freeform Laser Consolidated H13 and CPM 9V Tool Steels,” Metallogr. Microstruct. Anal., vol. 2, no. 2. pp. 67–78, 2013.

[50]. J. Mazumder, A. Schifferer, and J. Choi, “Direct materials deposition: designed macro and microstructure,” Mater. Res. Innov., vol. 3, pp. 118–131, 1999.

[51]. J. Choi, Y. Chang, “Characteristics of laser aided direct metal/material deposition process for tool steel,” Int. J. Mach. Tool Manuf., vol. 45, no. 4-5, pp. 597–607, 2005.

[52]. A. J. Pinkerton and L. Li, “Direct additive laser manufacturing using gas- and water-atomised H13 tool steel powders,” Int. J. Adv. Manuf. Technol., vol. 25, no. 5–6, pp. 471–479, 2005.

[53]. J. S. Park, J. H. Park, M. G. Lee, J. H. Sung, K. J. Cha, and D. H. Kim, “Effect of Energy Input on the Characteristic of AISI H13 and D2 Tool Steels Deposited by a Directed Energy Deposition Process,” Metall. Mater. Trans. A Phys. Metall. Mater. Sci., vol. 47, no. 5, pp. 2529–2535, 2016.

[54]. H. Chandler, “Heat Treaters’s Guide: Practices and Procedures for Irons and Steels, 2nd ed.,” ASM International, Materials Park, pp. 561–563, 1995.

[55]. J. Boes, A. Röttger, C. Mutke, C. Escher, and W. Theisen, “Microstructure and mechanical properties of X65MoCrWV3-2 cold-work tool steel produced by selective laser melting,” Addit. Manuf., vol. 23, no. July, pp. 170–180, 2018.

[56]. Z. H. Liu, D. Q. Zhang, C. K. Chua, K. F. Leong, “Crystal structure analysis of M2 high speed steel parts produced by selective laser melting,” Mater. Char., vol. 84, pp. 72–80, 2013.

[57]. K. Kempen, B. Vrancken, S. Buls, L. Thijs, J. Van Humbeeck, J.-P. Kruth, “Selective laser melting of crack-free high density M2 high speed steel parts by baseplate preheating,” J. Manuf. Sci. Eng., Vol. 136, pp. 061026, 2014.

[58]. J. Saewe, C. Gayer, L. Jauer, J. Kunz, C. Broeckmann, and J. H. Schleifenbaum, “Feasibility investigation for laser powder bed fusion of high-speed steels,” Euro PM 2018 Congress and Exhibition. 2020.

[59]. A. B. Spierings, N. Herres, and G. Levy, “Influence of the particle size distribution on surface quality and mechanical properties in AM steel parts,” Rapid Prototyp. J., vol. 17, no. 3, pp. 195–202, 2011.

[60]. G. Casalino, S. L. Campanelli, N. Contuzzi, and A. D. Ludovico, “Experimental investigation and statistical optimisation of the selective laser melting process of a maraging steel,” Opt. Laser Technol., vol. 65, pp. 151–158, 2015.

[61]. T. Mukherjee, J. S. Zuback, A. De, T. DebRoy, “Printability of alloys for additive manufacturing”. Sci. Rep., vol. 6, no. 1, pp. 1-8, 2016.

[62]. R. C. Barclay, “Parameter optimization for controlling aluminum loss when laser depositing Ti-6Al-4V,” Missouri University of Science and Technology, 2013.

[63]. A. Bauereiß, T. Scharowsky, and C. Körner, “Defect generation and propagation mechanism during additive manufacturing by selective beam melting,” J. Mater. Process. Technol., vol. 214, no. 11. pp. 2522–2528, 2014.

[64]. R. Cunningham et al., “Keyhole threshold and morphology in laser melting revealed by ultrahigh-speed x-ray imaging,” Science, vol. 363, no. 6429. pp. 849–852, 2019.

[65]. L. Thijs, F. Verhaeghe, T. Craeghs, J. Van Humbeeck, and J. P. Kruth, “A study of the microstructural evolution during selective laser melting of Ti-6Al-4V,” Acta Mater., vol. 58, no. 9. pp. 3303–3312, 2010.

[66]. D. Herzog, V. Seyda, E. Wycisk, C. Emmelmann, “Additive manufacturing of metals,” Acta Mater. Vol. 117, pp. 371–392, 2016.

[67]. C. Zhao, N. D. Parab, X. Li, K. Fezzaa, W. Tan, A. D. Rollett, & T. Sun, “Critical instability at moving keyhole tip generates porosity in laser melting,” Science, vol. 370, no. 6520, pp. 1080–1086, 2020

[68]. J. W. Elmer, J. Vaja, H. D. Carlton, and R. Pong, “The effect of Ar and N2 shielding gas on laser weld porosity in steel, stainless steels, and nickel,” Weld. J., vol. 94, no. 10. pp. 313s-325s, 2015.

[69]. C. PAUZON, “Tailored process gases for laser powder bed fusion.” Chalmers University of Technology, 2021.

[70]. F. Carter Giles, Materials science & engineering, Materials Park, Ohio:ASM International, 1991, ISBN 9780871703996.

[71]. S. Kou, “A criterion for cracking during solidification,” Acta Mater., vol. 88. pp. 366–374, 2015.

[72]. J. Liu and S. Kou, “Effect of diffusion on susceptibility to cracking during solidification,” Acta Mater., vol. 100. pp. 359–368, 2015.

[73]. H. Hyer et al., “Composition-dependent solidification cracking of aluminum-silicon alloys during laser powder bed fusion,” Acta Mater., vol. 208, p. 116698, 2021.

[74]. J. Krell, A. Röttger, K. Geenen, and W. Theisen, “General investigations on processing tool steel X40CrMoV5-1 with selective laser melting,” J. Mater. Process. Technol., vol. 255, no. June 2017, pp. 679–688, 2018.

[75]. P. Bajaj, A. Hariharan, A. Kini, P. Kürnsteiner, D. Raabe, and E. A. Jägle, “Steels in additive manufacturing: A review of their microstructure and properties,” Mater. Sci. Eng. A, vol. 772, no. November 2019, 2020.

[76]. F. Huber et al., “Laser beam melting and heat-treatment of 1.2343 (AISI H11) tool steel – microstructure and mechanical properties,” Mater. Sci. Eng. A, vol. 742, no. November 2018, pp. 109–115, 2019.

[77]. J. H. Martin, B. D. Yahata, J. M. Hundley, J. A. Mayer, T. A. Schaedler, and T. M. Pollock, “3D printing of high-strength aluminium alloys,” Nat. Publ. Gr., vol. 549, no. 7672, pp. 365–369, 2017.

[78]. https://microscopynook.com/microscopeTypes/scanningelectron.html

[79]. O. C. Wells, “Scanning Electron Microscopy,” Encyclopedia of Materials: Science and Technology, pp. 8265-8269, 2001.

[80]. A. E384-17, Standard Test Method for Microindentation Hardness of MAterials, West Conshohocken, PA: ASTM International, 2017.

[81]. E. Louvis, P. Fox, and C. J. Sutcliffe, “Selective laser melting of aluminium components,” J. Mater. Process. Technol., vol. 211, no. 2, pp. 275–284, 2011.